Banner appropriate to article type will appear here in typeset article

A consistent treatment of dynamic contact angles in the sharp-interface framework with the generalized Navier boundary condition

Tomas Fullana[1,2], Yash Kulkarni[1], Mathis Fricke[3], Stéphane Popinet[1], Shahriar Afkhami[4], Dieter Bothe[3], and Stéphane Zaleski[1,5]

[1]Sorbonne Université and CNRS, Institut Jean Le Rond d'Alembert UMR 7190, F-75005 Paris, France

[2]Laboratory of Fluid Mechanics and Instabilities, EPFL, Lausanne CH-1015, Switzerland

[3]Department of Mathematics, TU Darmstadt, Schlossgartenstraße 7, 64289 Darmstadt, Germany

[4]Department of Mathematical Sciences, New Jersey Institute of Technology, Newark, NJ, USA 07102

[5]Institut Universitaire de France, Paris, France

(Received xx; revised xx; accepted xx)

In this work, we revisit the Generalized Navier Boundary condition (GNBC) introduced by Qian et al. in the sharp interface Volume-of-Fluid context. We replace the singular uncompensated Young stress by a smooth function with a characteristic width ε that is understood as a physical parameter of the model. Therefore, we call the model the "Contact Region GNBC" (CR-GNBC). We show that the model is consistent with the fundamental kinematics of the contact angle transport described by Fricke, Köhne and Bothe. We implement the model in the geometrical Volume-of-Fluid solver Basilisk using a "free contact angle" method. This means that the dynamic contact angle is not prescribed but reconstructed from the interface geometry and subsequently applied as an input parameter to compute the uncompensated Young stress. We couple this approach to the two-phase Navier Stokes solver and study the withdrawing tape problem with a receding contact line. It is shown that the model is grid-independent and leads to a full regularization of the singularity at the moving contact line. In particular, it is shown that the curvature at the moving contact line is finite and mesh converging. We derive the thin film equation for the CR-GNBC and theoretically justify the finite curvature at the contact line. As predicted by the fundamental kinematics, the parallel shear stress component vanishes at the moving contact line for quasi-stationary states (i.e. for $\dot{\theta}_{\mathrm{d}} = 0$) and the dynamic contact angle is determined by a balance between the uncompensated Young stress and an effective contact line friction. Away from the moving contact line, we confirm that the viscous bending of the interface is well-described by the asymptotic theory of Cox. A non-linear generalization of the model is proposed, which allows to reproduce the Molecular Kinetic Theory of Blake and Haynes for quasi-stationary states.

Key words: dynamic contact line, Volume-of-Fluid method, Generalized Navier Boundary Condition, withdrawing plate, forced dewetting

Abstract must not spill onto p.2

1. Introduction

The phenomenon of dynamic wetting / dewetting requires a relative motion of the contact line, i.e. the triple line at which the liquid-fluid interface and the solid support's surface meet, against the solid wall. This fundamental process can be modeled in various ways. If the fluid-interface and the contact line are modeled as a material surface and a material line, respectively, it is clear that the classical no-slip condition is incompatible with the dynamic wetting process. Mathematically, it has been shown that, for a material interface and contact line, the no-slip boundary condition leads to a discontinuity in the velocity as the contact line is approached. Because of that, a viscous fluid develops a non-integrable singularity at the moving contact line. This has been first shown in the seminal paper by Huh & Scriven (1971). Since then, various mathematical models have been developed to resolve the paradox in the continuum mechanical description. In the framework of diffuse interface models, where both the fluid interface and contact line have a finite width characterized by a smooth but rapidly varying order parameter, a motion of the contact line can be achieved by pure diffusion of the order parameter; see Jacqmin (2000). In this case, the motion is driven by gradients of the chemical potential and the contact line is not a material line with respect to the fluid particles. The Interface Formation Model due to Shikhmurzaev (1993, 2008) describes the dynamic wetting process using mass transfer between the bulk phases of the liquid and the interfaces between fluid and solid and fluid gas. Hence, in this case, the contact line can move without hydrodynamic slip as the primary mechanism.

A commonly used approach in the sharp interface framework is to model the interface and the contact line as material objects and to allow for slip between the bulk velocity and the solid wall. The Navier slip condition states that the amount of tangential slip is determined by a balance between the tangential component of the viscous stress (described by the viscous stress tensor **S**) and a sliding friction force between fluid particles and the solid surface according to

$$-\beta(\mathbf{v}_{\|} - \mathbf{U}_w) = (\mathbf{S}\mathbf{n}_{\partial\Omega})_{\|}. \tag{1.1}$$

This boundary condition introduces the slip length $L := \eta/\beta$ as the key parameter. Here η denotes the viscosity of the liquid and $\beta > 0$ is a coefficient describing the (sliding) friction between the liquid molecules and the solid surface. Within the Navier slip model, the slip length can be interpreted geometrically as the distance below the solid surface where the linearly extrapolated tangential velocity vanishes. It is well-known that the singularity at the moving contact line is only partially relaxed by the Navier slip condition. A logarithmic divergence as a function of the distance to the contact line still exists for the curvature and the pressure, as pointed out by Huh & Mason (1977). However, the singularity is transformed into an integrable one and, hence, physically meaningful solutions (at least for the macroscopic flow) are possible. The physical implications of the pressure singularity is debated in the literature. Shikhmurzaev (2006) argues that the pressure should remain finite because otherwise the model of an incompressible fluid would no longer be valid. On the other hand, it has been demonstrated that the Navier slip model is able to describe various wetting experiments in a satisfactory manner.

Besides the mobility of the contact line, the wettability of the solid surface is another key parameter for the physical system. It is usually characterized by the equilibrium contact angle θ_{e} that the free surface forms with the solid boundary in equilibrium. It can be computed from the surface tension of the liquid-gas, liquid-solid and solid-gas interfaces, using the equation introduced by Young (1805), viz.

$$\sigma \cos\theta_e + \sigma_{ls} - \sigma_{sg} = 0. \tag{1.2}$$

While the latter equation can be easily deduced from variational principles, the dynamics of the contact angle is a much more complex problem and a large variety of empirical models exist. Notably, there is one fundamental relation for the dynamics of the microscopic contact angle θ_d in the limit of slow velocities of the contact line, which is shared by many of these models:

$$-\zeta U_{cl} = \sigma(\cos\theta_d - \cos\theta_e). \tag{1.3}$$

Here U_{cl} denotes the normal speed of the contact line relative to the solid surface (positive for advancing and negative for a receding contact line) and ζ is the so-called "contact line friction" parameter. Equation (1.3) arises, for example, from the molecular kinetic theory of wetting in the limit of small capillary numbers, i.e. for a slow motion of the contact line (see Blake & Haynes (1969); Blake *et al.* (2015)).

Recently, Fricke *et al.* (2019, 2018) studied the fundamental kinematics of the contact angle transport and showed that the rate-of-change of the contact angle is fully determined by the directional tangential derivative of the velocity field $\mathbf{v}$ at the contact line, viz.

$$\dot{\theta}_d = (\partial_\tau \mathbf{v}) \cdot \mathbf{n}_\Sigma. \tag{1.4}$$

Here $\mathbf{n}_\Sigma$ denotes the interface normal vector and τ is a vector tangential to the interface (see Section 2 for more details). Notably, when applied to the full two-phase flow problem (assuming sufficient regularity of the solution), Equation (1.4) implies that $\dot{\theta}_d$ is proportional to the derivative in the direction normal to the wall of a tangential velocity component. In other words, (1.4) predicts an "apparent perfect slip" at the moving contact line if the contact angle does not change in time, i.e. if $\dot{\theta}_d = 0$. Indeed, indications of a vanishing shear stress in the vicinity of the contact line have been observed in molecular dynamics (MD) simulations by Thompson & Robbins (1989) and others. We will see below, that perfect slip in the sense of vanishing shear-stress is possible within GNBC model which makes the model consistent with equation (1.4). On the other hand, Fricke *et al.* (2019); Fricke & Bothe (2020) showed that the Navier slip model (1.1) with a contact angle boundary condition like (1.3) is not consistent with (1.4) and regular solutions (if they exist) show an unphysical behavior.

The "Generalized Navier Boundary Condition" (GNBC) was first described by Qian *et al.* (2003, 2006*a*,*b*) in the context of diffuse interface models. The key idea of the GNBC is to introduce the *uncompensated Young stress* as an additional force density into the constitutive relation (1.1). So, in this model, the slip velocity relative to the solid surface is a result of a balance between a sliding friction force, the viscous stress and the uncompensated Young stress. In a sharp interface and sharp contact line formulation, the GNBC can be written as (see Gerbeau & Lelièvre (2009))

$$-\beta(\mathbf{v}_\parallel - \mathbf{U}_w) = (\mathbf{S}\mathbf{n}_{\partial\Omega})_\parallel + \sigma(\cos\theta_d - \cos\theta_e)\,\mathbf{n}_\Gamma \delta_\Gamma \quad \text{on} \quad \partial\Omega. \tag{1.5}$$

Notably, the contact line delta distribution δ_Γ appears because, in the sharp contact line formulation, the Young stress is concentrated just on a mathematical curve. Hence, Equation (1.5) should mathematically be understood as an equality of distributions. This delta function GNBC formulation is applicable in weak formulations of the two-phase flow problem where the contact line delta distribution will translate into an integral over the contact line in the weak formulation (see, e.g, Gerbeau & Lelièvre (2009); Fumagalli *et al.* (2018)). On the other hand, there is no contact line delta distribution in the Phase Field formulation of the

GNBC due to Qian et al., because the thickness of the interface and the contact line is a finite, physical model parameter in this case. Yamamoto *et al.* (2013, 2014) implemented the GNBC approach into a front-tracking-method and studied the dynamics of capillary rise in a tube. In this method, the contact line is transported by an advection of the Lagrangian marker points without a prescribed contact angle. Then the dynamic contact angle is evaluated and used to compute the uncompensated Young stress, which determines the slip velocity profile. Yamamoto et al. noticed that the viscous stress becomes negligible as the contact line is approached. Motivated by this observation, they dropped the viscous stress contribution in (1.5) leading to a "simplified GNBC", formally reading as

$$-\beta(\mathbf{v}_{\parallel} - \mathbf{U}_w) = \sigma(\cos\theta_{\mathrm{d}} - \cos\theta_{\mathrm{e}})\, \mathbf{n}_\Gamma \delta_\Gamma. \tag{1.6}$$

It is evident that, by taking the inner product with the contact line normal vector, Eq. (1.6) can be formally reduced to an equation equivalent to (1.3) if the delta distribution is approximated with a regular function over a finite width. Indeed, Yamamoto *et al.* (2013, 2014) smoothed the delta distribution over a region of approximately four grid points. Using this estimate as the characteristic width of the delta function, the authors concluded that

$$U_{\mathrm{cl}} \approx \frac{\lambda}{\Delta} \frac{\sigma(\cos\theta_{\mathrm{e}} - \cos\theta_{\mathrm{d}})}{\eta}, \tag{1.7}$$

where Δ is the grid size. Obviously, the contact line speed in (1.7) can only be grid-independent if also the slip length is chosen in proportion to the grid size, i.e. if $\lambda \sim \Delta$. Consequently, they fixed the parameter $\chi := \lambda/\Delta$ in their simulations. The approach was extended by using the Cox-Voinov relation for θ_{d} in Yamamoto *et al.* (2014). Later, Yamamoto *et al.* (2016) used this method to study the withdrawing plate problem with a single wettable defect. Recently, the GNBC front-tracking approach was extended by Kawakami *et al.* (2023) using a so-called "rolling belt-model" inspired by the work of Lukyanov & Pryer (2017). Chen *et al.* (2019) used the GNBC in a Front Tracking method to study the coalescence-induced self-propelled motion of droplets on a solid surface. Shang *et al.* (2018) used a quite similar method to study droplet spreading and the motion of drops on surfaces subject to a shear flow. All these methods have in common that the uncompensated Young stress is distributed over a characteristic distance, which is related to the mesh size.

In the present work, we propose a "sharp-interface, contact region GNBC" (CR-GNBC) formulation, where the contact line delta distribution is replaced by a smooth function with a characteristic width $\varepsilon > 0$. This width ε is understood as a physical model parameter and is, therefore, chosen independently of the computational mesh. It has been shown recently by Kulkarni *et al.* (2023) that this model (i.e. the GNBC model with finite ε) admits a local C^2-regularity of the velocity in the vicinity of the moving contact line. We develop an implementation of the CR-GNBC in a geometrical Volume-of-Fluid method. This method should be consistent with the fundamental kinematic law (1.4). Therefore, the dynamic contact angle is not prescribed but is reconstructed from the volume fraction field in a neighborhood of the contact line. As one important preliminary step, we validate this "free contact angle" method by studying the advection problem by a *prescribed* velocity field (see Fricke *et al.* (2020)). In this case, the interface and the contact line are transported without a boundary condition for the contact angle and the results are validated against analytical solutions of (1.4). We couple this method to the CR-GNBC model and use the reconstructed contact angle θ_{d} as an input parameter to compute the uncompensated Young stress in the simulation.

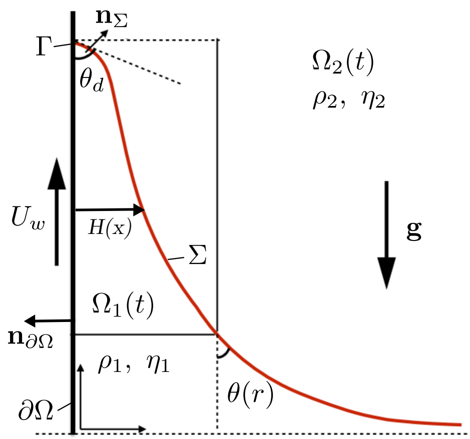

Figure 1: Mathematical notation for the withdrawing tape setup.

Structure of this article

We study the withdrawing tape problem as a prototypical example for a dynamic dewetting process. The setup follows the previous work by Afkhami *et al.* (2018). The solid wall is moving upwards with velocity $U_w \geqslant 0$ in the laboratory frame (see Figure 1). So, we study the case of a receding contact line. We define the (global) capillary number with respect to the wall speed as

$$\text{Ca} := \frac{\eta U_w}{\sigma}. \tag{1.8}$$

For convenience, we define the *contact line* capillary number using the negative contact line speed, i.e. (note that the contact line speed U_{cl} is always measured relative to the solid)

$$\text{Ca}_{\text{cl}} := \frac{\eta(-U_{\text{cl}})}{\sigma}. \tag{1.9}$$

In a quasi-stationary state, we have $-U_{\text{cl}} = U_w$ and hence $\text{Ca} = \text{Ca}_{\text{cl}}$. With this definition, we can always work with positive values for the capillary number. Notice that, in the literature, one will also find the convention that Ca_{cl} is negative for a receding contact line and positive for an advancing contact line.

The mathematical derivation of the GNBC in a sharp-interface framework is revisited in Section 2. It is shown that the GNBC can be obtained as a combined closure relation for the dissipation due to slip along the liquid-solid surface and the contact line dissipation. Using the laws of kinematics, we derive the contact angle evolution equation in Section 2.4 and show that (1.3) holds for quasi-stationary states. Moreover, the GNBC thin film equation is derived in Section 2.5. The numerical implementation of the method in the geometrical Volume-of-Fluid solver is described in Section 3. We validate the numerical method by studying the kinematic transport of the contact angle and the curvature at the contact line. The results for the withdrawing tape problem are discussed in detail in Section 4. In particular, it is shown that the results are mesh converging. Notably, we can demonstrate by a mesh study that, unlike for the Navier slip model, the curvature at the contact line converges to a finite value. Away from the contact line, we show that the viscous bending

Table 1: List of Symbols

Symbol	Description	Units
ρ	Density	kg/m^3
η	Viscosity	Pa·s
σ	Surface Tension	N/m
$\mathbf{v}$	Velocity	m/s
β	Friction Coefficient	Pa·s/m
$\mathbf{g}$	Gravitational Acceleration	m/s^2
$\mathbf{D}$	Rate-of-Deformation Tensor	1/s
$\mathbf{S} = 2\eta\mathbf{D}$	Viscous Stress Tensor	Pa
Σ	Interface	-
V_Σ	Interface Normal Speed	m/s
$\mathbf{n}_\Sigma$	Interface Normal	-
$\kappa = -\nabla_\Sigma \cdot \mathbf{n}_\Sigma$	Interface Mean Curvature	1/m
Γ	Contact Line	-
U_{cl}	Contact Line Speed	m/s
$\mathbf{n}_\Gamma$	Contact Line Normal (tangential to $\partial\Omega$)	-
$\partial\Omega$	Solid Boundary	-
$\mathbf{n}_{\partial\Omega}$	Unit Outer Normal to Ω	-
U_w	Wall Speed	m/s
$\mathbf{U}_w$	Wall Velocity	m/s
$\lambda = \eta/\beta$	Slip Length	m
Ca	Wall Capillary Number	-
$\mathrm{Ca}_{\mathrm{cl}}$	Contact Line Capillary Number	-
$\mathrm{Ca}_{\mathrm{loc}}$	Capillary Number in the lab frame of reference	-
$\mathrm{Ca}_{\mathrm{tr}}$	Transition Capillary Number	-
ζ	Contact Line Friction	Pa·s
θ_{e}	Static Contact Angle	rad
θ_{d}	Dynamic Microscopic Contact Angle	rad
θ_Δ	Numerical contact angle observed at the contact line	rad
θ_{s}	Steady state contact angle	rad

of the interface is well-described by the hydrodynamic theory of Cox. Finally, we conclude this study by an outlook to a non-linear variant of the GNBC, which can be derived as a non-linear closure of the entropy production described earlier in Section 2.

2. Mathematical Modeling

2.1. *Governing equations*

We employ the sharp-interface continuum modeling approach. We start from the incompressible, two-phase Navier Stokes equations with surface tension for Newtonian fluids under isothermal conditions (see, e.g., Slattery (1999); Prüss & Simonett (2016)). Inside the fluid phases, the governing equations are

$$\partial_t(\rho\mathbf{v}) + \nabla\cdot(\rho\mathbf{v}\otimes\mathbf{v}) + \nabla p = \nabla\cdot\mathbf{S} + \rho\mathbf{g}, \tag{2.1}$$

$$\nabla\cdot\mathbf{v} = 0 \tag{2.2}$$

with the viscous stress tensor†

$$\mathbf{S} = 2\eta\mathbf{D} = \eta(\nabla\mathbf{v} + \nabla\mathbf{v}^{\mathsf{T}}).$$

These bulk equations are accompanied by jump conditions at the interface $\Sigma(t)$. The interface is modeled as a hypersurface (i.e. it has zero thickness) and separates the domain Ω into two bulk phases $\Omega_{1,2}(t)$ occupied by the two fluid phases (see Fig. 1). Assuming that no phase change occurs in the system, the normal component of the adjacent fluid velocities $\mathbf{v}_{1,2}$ at the interface are coinciding and equal to the speed of normal displacement V_Σ of the interface, resulting in the kinematic boundary condition

$$V_\Sigma = \mathbf{v} \cdot \mathbf{n}_\Sigma \quad \text{on} \quad \Sigma(t), \tag{2.3}$$

where $\mathbf{n}_\Sigma$ is the interface unit normal field. Additionally, no-slip between the fluid phases is usually assumed. Assuming further that the surface tension σ is constant, the jump conditions for mass and momentum read as

$$[\![\mathbf{v}]\!] = 0, \quad [\![p\mathbb{I} - \mathbf{S}]\!]\,\mathbf{n}_\Sigma = \sigma\kappa\mathbf{n}_\Sigma \quad \text{on} \quad \Sigma(t). \tag{2.4}$$

Here $\kappa := -\nabla_\Sigma \cdot \mathbf{n}_\Sigma$ is twice the mean curvature of the interface and

$$[\![\psi]\!]\,(t,\mathbf{x}) := \lim_{h\to 0^+} (\psi(t,\mathbf{x} + h\mathbf{n}_\Sigma) - \psi(t,\mathbf{x} - h\mathbf{n}_\Sigma))$$

is the jump of a quantity ψ across the interface. We assume that the solid boundary $\partial\Omega$ is not able to store mass and we assume it to be impermeable. We consider an inertial frame of reference, where the wall is moving parallel to itself with a velocity $U_w \geqslant 0$ upwards (see Fig. 1). The impermeability condition in this frame of reference reads as

$$\mathbf{v}_\perp = 0 \quad \text{on } \partial\Omega, \tag{2.5}$$

where $\mathbf{v}_\perp = (\mathbf{v} \cdot \mathbf{n}_{\partial\Omega})\,\mathbf{n}_{\partial\Omega}$ denotes the normal part of the velocity with respect to $\partial\Omega$.

In order to obtain a closed model, the system of equations (2.1)-(2.5) must be complemented by (one or more) additional boundary conditions describing

(i) the **wettability** of the solid (i.e. the static and dynamic contact angle) and

(ii) the **mobility** of the contact line (i.e. the tangential velocity $\mathbf{v}_{||}$ at the solid boundary).

These boundary conditions are closure relations for the continuum mechanical description and must be thermodynamically consistent, i.e. they must obey in particular the second law of thermodynamics. To arrive at a consistent closure, we consider the available energy consisting of the kinetic energy of the bulk phases and the surface energies of the liquid-gas interface as well as the wetted area $W(t) \subset \partial\Omega$, i.e.

$$E(t) := \int_{\Omega\setminus\Sigma(t)} \frac{\rho|\mathbf{v}|^2}{2}\, dV + \int_{\Sigma(t)} \sigma\, dA + \int_{W(t)} \sigma_w\, dA.$$

Here $\sigma = \sigma_{\mathrm{lg}} > 0$ denotes the surface tension of the liquid-gas interface and

$$\sigma_{\mathrm{w}} = \sigma_{\mathrm{ls}} - \sigma_{\mathrm{sg}}$$

is the specific energy density for wetting the solid surface. Note that σ_{w} might be negative, as we see from Young's equation

$$\sigma \cos\theta_{\mathrm{e}} + \sigma_{\mathrm{w}} = 0, \tag{2.6}$$

which defines the "static" or "equilibrium" contact angle θ_{e}. It is a purely mathematical exercise (see Fricke (2021) (Appendix A) for details) to compute the rate of change $\dot{E}$ for a

† We use the symbol $\mathbf{D} = \frac{1}{2}(\nabla\mathbf{v} + \nabla\mathbf{v}^{\mathsf{T}})$ for the rate-of-deformation tensor.

sufficiently regular solution of (2.1)-(2.5) (in the absence of external forces, i.e. for $\mathbf{g} = 0$). The result reads as

$$\frac{dE}{dt} = -\int_{\Omega\setminus\Sigma(t)} \mathbf{S} : \mathbf{D}\, dV + \int_{\partial\Omega} (\mathbf{v}_{\|} - \mathbf{U}_w) \cdot (\mathbf{S}\mathbf{n}_{\partial\Omega})_{\|}\, dA + \int_{\Gamma(t)} \sigma(\cos\theta_{\mathrm{d}} - \cos\theta_{\mathrm{e}})\, U_{\mathrm{cl}}\, dl. \tag{2.7}$$

In this formulation with a continuous velocity field, the scalar contact line speed (measured relative to the solid) is given as

$$U_{\mathrm{cl}} = \mathbf{v} \cdot \mathbf{n}_\Gamma - U_w.$$

Closure relations are required to satisfy the second law of thermodynamics† $\dot{E} \leqslant 0$. The first contribution in (2.7) has a negative sign as we consider incompressible Newtonian fluids, i.e. $\mathbf{S} = 2\eta\mathbf{D}$. A linear closure for the second integral in (2.7) yields the well-known Navier slip condition, i.e.

$$-\beta(\mathbf{v}_{\|} - \mathbf{U}_w) = (\mathbf{S}\mathbf{n}_{\partial\Omega})_{\|} \quad \text{with a friction coefficient} \quad \beta \geqslant 0. \tag{2.8}$$

Using the slip length parameter $\lambda = \eta/\beta$, one may reformulate (2.8) as

$$\mathbf{v}_{\|} + 2\lambda(\mathbf{D}\mathbf{n}_{\partial\Omega})_{\|} = \mathbf{U}_w. \tag{2.9}$$

The third integral in (2.7) suggests that the dynamic contact angle θ_{d}, which is *mathematically* defined as the angle of intersection‡ of the free surface Σ with the solid boundary $\partial\Omega$, i.e.

$$\cos\theta_d := -\mathbf{n}_\Sigma \cdot \mathbf{n}_{\partial\Omega} \quad \text{at } \Gamma(t),$$

should be linked to the contact line speed U_{cl}. A linear closure leads to the well-known condition

$$-\zeta U_{\mathrm{cl}} = \sigma(\cos\theta_{\mathrm{d}} - \cos\theta_{\mathrm{e}}) \quad \text{with a (contact line) friction coefficient} \quad \zeta \geqslant 0. \tag{2.10}$$

Note that also more general contact angle boundary conditions are possible if a non-linear closure relation is employed. To summarize, the “standard model”¶ based on the Navier slip condition is given by Equations (2.1)-(2.5), (2.9) together with (2.10) or a non-linear variant of the form

$$\theta_{\mathrm{d}} = f(U_{\mathrm{cl}}) \quad \text{on} \quad \Gamma(t). \tag{2.11}$$

To ensure thermodynamic consistency, we require that

$$\eta \geqslant 0, \quad \sigma \geqslant 0, \quad \lambda \geqslant 0, \quad U_{\mathrm{cl}}(f(U_{\mathrm{cl}}) - \theta_{\mathrm{e}}) \geqslant 0.$$

As shown by Fricke & Bothe (2020), there is an inconsistency of boundary conditions in the standard model because the evolution of the contact angle is determined by the contact angle boundary condition (say (2.10)) *as well as* by the flow in the vicinity of the contact line according to (1.4). As a consequence, a regular solution of the system does not exist but a weak singularity is present at the contact line as shown already in Huh & Mason (1977).

† Note that we assume an isothermal system here. In this case, we may directly consider the change in available energy.

‡ Note that, in order to define the contact angle θ_{d}, we have to assume that interface $\Sigma(t)$ has a well-defined normal field up to the boundary. This is the case even if the curvature has a logarithmic, hence integrable, singularity.

¶ The mathematical model (2.1)-(2.5), (2.9), (2.10) is one of the most commonly applied models for dynamic wetting in the literature. However, there are many more modeling approaches which aim at a regularization of the singularity and a prediction of the dynamics of wetting. For a survey of the field, we refer to the references de Gennes *et al.* (2004); Blake (2006); Shikhmurzaev (2008); Bonn *et al.* (2009); Snoeijer & Andreotti (2013*a*); Marengo & De Coninck (2022).

2.2. *Formal derivation of the GNBC*

It is important to note that the GNBC was originally formulated in a *diffuse* interface framework (see Qian *et al.* (2003, 2006*a*)). However, the GNBC can be formally understood in the sharp interface model as a *combined closure* for the terms in the entropy production (2.7) which arises from the contact line motion and from slip at the solid-liquid boundary. The combined closure leads to a single boundary condition instead of the two independent conditions in the standard Navier slip model. Hence, the number of boundary conditions is reduced and one can show that the inconsistency at the contact line is resolved (see below).

As a starting point, we consider the sum of the wall and the contact line dissipation, given as

$$\mathcal{T} = \int_{\partial\Omega} (\mathbf{v}_{\|} - \mathbf{U}_w) \cdot (\mathbf{S}\mathbf{n}_{\partial\Omega})_{\|}\, dA + \sigma \int_{\Gamma(t)} (\cos\theta_{\mathrm{d}} - \cos\theta_{\mathrm{e}})\, U_{\mathrm{cl}}\, dl.$$

By introducing the contact line delta distribution δ_Γ, one can rewrite $\mathcal{T}$ as a single integral over the entire solid boundary $\partial\Omega$ according to

$$\mathcal{T} = \int_{\partial\Omega} \left((\mathbf{S}\mathbf{n}_{\partial\Omega})_{\|} + \sigma(\cos\theta_{\mathrm{d}} - \cos\theta_{\mathrm{e}})\, \mathbf{n}_\Gamma \delta_\Gamma\right) \cdot (\mathbf{v}_{\|} - \mathbf{U}_w)\, dA.$$

Note that it is possible to factor out the common co-factor $(\mathbf{v}_{\|} - \mathbf{U}_w)$ because the contact line speed can be written as $U_{\mathrm{cl}} = (\mathbf{v}_{\|} - \mathbf{U}_w) \cdot \mathbf{n}_\Gamma$. A *linear*† closure relation is now provided by the generalized Navier boundary condition

$$-\beta(\mathbf{v}_{\|} - \mathbf{U}_w) = (\mathbf{S}\mathbf{n}_{\partial\Omega})_{\|} + \sigma(\cos\theta_{\mathrm{d}} - \cos\theta_{\mathrm{e}})\, \mathbf{n}_\Gamma \delta_\Gamma \quad \text{on} \quad \partial\Omega \tag{2.12}$$

with a friction coefficient $\beta > 0$. Notice that the "delta function GNBC" should be understood in the sense of distributions.

2.3. *Contact Region GNBC (CR-GNBC) model*

To obtain the CR-GNBC model, we replace the contact line delta distribution in (2.12) by a smooth function defined over a finite transition region with characteristic width ε such that

$$\delta_\Gamma^\varepsilon \geqslant 0, \qquad \int \delta_\Gamma^\varepsilon(x)\, \mathrm{d}x = 1.$$

Note that this approach also requires to extend the definition of the contact angle θ_{d} and the contact line normal $\mathbf{n}_\Gamma$ away from the sharp contact line. In fact, the existence of the solid boundary, touching the interface at an angle strictly between 0 and π, provides a means for this extension of the contact line to a finite region. Then, the deviation of the contact angle from the equilibrium value appears in the velocity boundary condition leading to a balance between sliding friction forces due to slip along the solid boundary, the tangential component of the viscous stress at the boundary and the uncompensated Young force:

$$-(\mathbf{v}_{\|} - \mathbf{U}_w) = 2\lambda(\mathbf{D}\mathbf{n}_{\partial\Omega})_{\|} + \frac{\sigma}{\beta}[(\cos\theta_{\mathrm{d}} - \cos\theta_{\mathrm{e}})\, \mathbf{n}_\Gamma \delta_\Gamma^\varepsilon]. \tag{2.13}$$

Notably, the dynamic contact angle is not prescribed explicitly in this approach. Instead, the dynamics of the contact angle is determined by (2.13) and the kinematics of the interface transport.

† A non-linear generalization of the closure is discussed in Section 6.

2.4. *Kinematics of the dynamic contact angle*

We derive the evolution law for the contact angle, given a sufficiently regular solution of the CR-GNBC model (2.1)-(2.5) and (2.13). Below, we consider the limit of the free surface case, where one phase is assumed to be a dynamically passive gas at a constant pressure. We assume that $\delta_\Gamma^\varepsilon$ evaluated at the contact line yields a value of $1/\varepsilon$. Then, the CR-GNBC condition, evaluated at the contact line, reads as

$$\beta(\mathbf{v}_{\parallel} - \mathbf{U}_w) + (\mathbf{S}\mathbf{n}_{\partial\Omega})_{\parallel} + \frac{1}{\varepsilon}\sigma(\cos\theta_{\mathrm{d}} - \cos\theta_{\mathrm{e}})\,\mathbf{n}_\Gamma = 0 \quad \text{at} \quad \Gamma. \tag{2.14}$$

By taking the inner product with the contact line normal vector $\mathbf{n}_\Gamma$ (normal to the contact line and tangential to the solid), we obtain the relation

$$\frac{U_{\mathrm{cl}}}{\lambda} + \langle \mathbf{n}_\Gamma, (\nabla\mathbf{v})\,\mathbf{n}_{\partial\Omega}\rangle + \langle (\nabla\mathbf{v})\,\mathbf{n}_\Gamma, \mathbf{n}_{\partial\Omega}\rangle + \frac{\sigma}{\varepsilon\eta}(\cos\theta_{\mathrm{d}} - \cos\theta_{\mathrm{e}}) = 0 \quad \text{at}\ \Gamma. \tag{2.15}$$

Using the kinematic evolution equation for the contact angle derived in Fricke *et al.* (2019), one can show that the rate-of-change of the contact angle $\dot{\theta}_{\mathrm{d}}$ is given as

$$2\dot{\theta}_{\mathrm{d}} = -\langle \mathbf{n}_\Gamma, (\nabla\mathbf{v})\,\mathbf{n}_{\partial\Omega}\rangle\,. \tag{2.16}$$

Moreover, it follows from the impermeability condition that the term $\langle \nabla\mathbf{v}\,\mathbf{n}_\Gamma, \mathbf{n}_{\partial\Omega}\rangle$ vanishes for a flat solid boundary. Therefore, we obtain the contact angle evolution law for a regular solution of the CR-GNBC model. It reads as

$$\boxed{\dot{\theta}_{\mathrm{d}} = \frac{U_{\mathrm{cl}}}{2\lambda} + \frac{1}{\varepsilon}\frac{\sigma}{2\eta}(\cos\theta_{\mathrm{d}} - \cos\theta_{\mathrm{e}}).} \tag{2.17}$$

Remarks

(i) Compared to the standard Navier slip model (see Fricke *et al.* (2019) for details), the uncompensated Young stress leads to an additional term in the equation for $\dot{\theta}_{\mathrm{d}}$, which reads as

$$\frac{1}{\varepsilon}\frac{\sigma}{2\eta}(\cos\theta_{\mathrm{d}} - \cos\theta_{\mathrm{e}}).$$

Obviously, the latter term is negative for $\theta_{\mathrm{d}} > \theta_{\mathrm{e}}$ (and positive for $\theta_{\mathrm{d}} < \theta_{\mathrm{e}}$) and, hence, drives the system towards equilibrium.

(ii) An important consequence of the CR-GNBC for *quasi-stationary* states is that it defines a functional dependence between the dynamic contact angle and the contact line speed. In fact, setting $\dot{\theta}_{\mathrm{d}} = 0$ leads to the relation

$$\mathrm{Ca}_{\mathrm{cl}} = \frac{\eta(-U_{\mathrm{cl}})}{\sigma} = \frac{\lambda}{\varepsilon}(\cos\theta_{\mathrm{d}} - \cos\theta_{\mathrm{e}}), \tag{2.18}$$

or, equivalently, to

$$-(\beta\varepsilon)\,U_{\mathrm{cl}} = \sigma(\cos\theta_{\mathrm{d}} - \cos\theta_{\mathrm{e}}). \tag{2.19}$$

By comparing (2.19) with (2.10), we see that the contact line friction parameter can be indentified with the product of the “bulk friction” in the Navier slip condition and the width of the contact line region, i.e.

$$\zeta = \beta\varepsilon. \tag{2.20}$$

The latter equation has been proposed before by Blake *et al.* (2015) in the context of the molecular kinetic theory. Physically, it indicates that, within the present modeling framework, there is only *one* friction mechanism that affects both the slip at the solid boundary and the

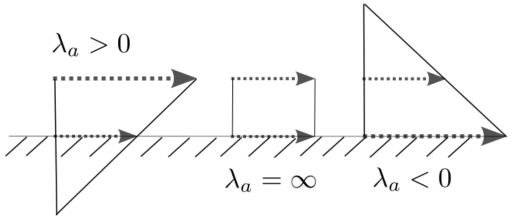

Figure 2: Different cases for the apparent slip length λ_a: positive, perfect and negative slip (reference frame with $U_w = 0$).

dynamics of the microscopic contact angle. In this sense, the contact line friction ζ can be understood as the lumped wall friction of the contact region.

(iii) From (2.16) we conclude that the stress component $\langle \mathbf{n}_\Gamma, (\nabla \mathbf{v})\, \mathbf{n}_{\partial\Omega} \rangle$ vanishes at the contact line for quasi-stationary states, i.e. for $\dot{\theta} = 0$. So, there appears to be "perfect slip" at the contact line in that case. Actually, the concepts of the "apparent slip length" λ_a (see Fig. 2) and the physical slip parameter defined as $\lambda = \eta/\beta$ must be distinguished for the GNBC model. In fact, the uncompensated Young stress is able to reverse the sign of the velocity gradient at the contact line. In this case, fluid particles at the solid boundary may have a larger tangential velocity than fluid particles slightly above the boundary. This situation corresponds to a *negative* apparent slip length (see Fig. 2). It is, however, caused by the uncompensated Young stress in the velocity boundary condition. The physical slip length parameter λ is still positive and finite in all cases.

(iv) Note that (2.17) can be phrased as a generalized mobility law of the form

$$U_{\mathrm{cl}} = f(\theta_{\mathrm{d}}, \dot{\theta}_{\mathrm{d}}). \tag{2.21}$$

Therefore, the contact line speed depends on the contact angle θ_{d} but also on its rate-of-change $\dot{\theta}_{\mathrm{d}}$ which, in turn, can be computed from $\nabla \mathbf{v}$ (see Fricke *et al.* (2019)). In this sense, the contact line speed in the GNBC model depends on the flow in the vicinity of the contact line.

(v) Moreover, the GNBC can be understood as an *inhomogeneous* Robin condition for the velocity. Hence, the GNBC enforces a flow whenever $\theta_{\mathrm{d}} \neq \theta_{\mathrm{e}}$. In contrast to the standard model, the GNBC model is able to describe the relaxation process of the contact angle.

2.5. *The CR-GNBC thin film equation*

We now derive the thin film equation for the CR-GNBC and compare it with other known thin film equations in the context of dynamic contact lines. The coordinate system is shown in Figure 1. Under the thin film assumption, we consider that the pressure remains constant along the y-axis and that the Laplace pressure jump across the interface can be expressed as

$$\Delta p = -\frac{\sigma H''}{(1 + H'^2)^{3/2}} \approx -\sigma H''.$$

The x-momentum equation

$$-\frac{1}{\rho}\frac{\partial p}{\partial x} + g + \frac{\eta}{\rho}\frac{\partial^2 v}{\partial y^2} = 0. \tag{2.22}$$

is supplemented by a free surface condition

$$\frac{\partial v}{\partial y}(x, H) = 0.$$

Since we are in the reference frame of the contact line, we can write the CR-GNBC as

$$v(x,0) + \lambda \frac{\partial v}{\partial y}(x,0) = U_w[1 - f\left(\frac{x}{\varepsilon}\right)], \tag{2.23}$$

where $f\left(\frac{x}{\varepsilon}\right)$ is the smoothed Dirac function that will be defined in (3.6). For further details on the formulation in the reference frame of the contact line, we refer to Kulkarni *et al.* (2023). Given the contact line boundary condition, the free surface condition and the Laplace pressure jump, the x-momentum equation (2.22) can now be written as an ordinary differential equation in terms of H

$$H^{'''} + \frac{1}{\mathrm{l_c}^2} = -\frac{3\,\mathrm{Ca}\left(1 - f\left(\frac{x}{\varepsilon}\right)\right)}{H(H-3\lambda)} - \frac{-3\eta Q}{\sigma H^2(H-3\lambda)}, \tag{2.24}$$

where $\mathrm{l_c}$ is the capillary length and $Q = -\int_0^H v\, ds$ is the total flux. Assuming steady state, where $Q = 0$, and in the vicinity of the contact line that $H^{'''} \gg 1/\mathrm{l_c}^2$ we obtain the CR-GNBC thin film equation

$$H^{'''} = \frac{3\,\mathrm{Ca}\left(\tanh^2\left(\frac{x}{\varepsilon}\right)\right)}{H(H-3\lambda)}. \tag{2.25}$$

From (2.25), we can see that for $x \ll \varepsilon$, $H^{''}$ does not diverge and approaches a constant value at the contact line ($x = 0$). Hence, the equation is singularity-free. Our CR-GNBC model can therefore be viewed as Navier slip with a *smoothening well* of width ε around the contact line where the uncompensated Young stress acts. A comparison of thin film equations from the literature and their respective smoothness in presented in Table 2.

3. Numerical Methods

3.1. *The Volume-of-Fluid method*

The Volume-of-Fluid (VOF) method for representing fluid interfaces coupled with a flow solver is well-known to be suited for solving interfacial flows (see e.g. Scardovelli & Zaleski (1999); Popinet & Zaleski (1999); Tryggvason *et al.* (2011); Marić *et al.* (2020)). We use the free software *Basilisk*, a platform for the solution of partial differential equations on adaptive Cartesian meshes (Popinet (2009, 2015, 2018)). For a two-phase flow, the volume fraction $c(\mathbf{x}, t)$ is defined as the integral of the first fluid's characteristic function in the control volume. The volume fraction $c(\mathbf{x}, t)$ is used to define the density and viscosity in the control volume according to

$$\begin{aligned} \rho(c) &\equiv c\rho_1 + (1-c)\rho_2, \\ \mu(c) &\equiv c\mu_1 + (1-c)\mu_2, \end{aligned} \tag{3.1}$$

with ρ_1, ρ_2 and μ_1, μ_2 the densities and viscosities of the phase 1 and 2 respectively.
The advection equation for the density is then replaced by the equation for the volume fraction

$$\partial_t c + \mathbf{v} \cdot \nabla c = 0. \tag{3.2}$$

The projection method is used to solve the incompressible Navier-Stokes equations combined with a Bell-Collela-Glaz advection scheme and a VOF method for interface tracking. The resolution of the surface tension term is directly dependent on the accuracy of the curvature calculation. The Height-Function method, described in Afkhami & Bussmann (2008, 2009), is a VOF-based technique for calculating interface normals and curvatures. About each

Table 2: Thin film equations for various contact line boundary conditions

Boundary condition	**Thin film equation form**	**Smoothness**
No slip: $v = U_w$	$H''' = \frac{1}{H^2}$ Duffy & Wilson (1997)	Singular H' (angle singularity)
Navier slip: $v - \lambda \frac{\partial v}{\partial y} = U_w$	$H''' = \frac{3\,\mathrm{Ca}}{H^2 + 3\lambda H}$ Eggers (2004)	Singular $H'' \sim \log x$ (curvature singularity)
Super-slip: $v - \lambda^2 \frac{\partial^2 v}{\partial y^2} = U_w$	$H''' = \frac{\mathrm{Ca}}{H^2 + \lambda^2}$ Hocking (2001)	Regular H'' (singularity-free)
Super-slip: $v - \lambda \frac{\partial v}{\partial y} - \lambda^2 \frac{\partial^2 v}{\partial y^2} = U_w$	$H''' = \frac{\mathrm{Ca}}{H^2/3 + \lambda H + \lambda^2}$ Devauchelle *et al.* (2007)	Regular H'' (singularity-free)
CR-GNBC	$H''' = \frac{3\,\mathrm{Ca}(\tanh^2 \frac{x}{\varepsilon})}{H(H - 3\lambda)}$ current paper	Regular H'' (singularity-free)

interface cell, fluid 'heights' are calculated by summing fluid volume in the grid direction closest to the normal of the interface. In two dimensions, a 7×3 stencil around an interface cell is constructed and the heights are evaluated by summing volume fractions horizontally, i.e.

$$h_j = \sum_{k=i-3}^{k=i+3} c_{j,k}\,\Delta, \tag{3.3}$$

with $c_{j,k}$ the volume fraction and Δ the grid spacing. The heights are then used to compute the interface normal $\mathbf{n}_\Sigma$ and the curvature κ according to

$$\begin{aligned} \mathbf{n}_\Sigma &= (h_x, -1), \\ \kappa &= \frac{h_{xx}}{\left(1 + h_x^2\right)^{3/2}}, \end{aligned} \tag{3.4}$$

where h_x and h_{xx} are discretized using second-order central differences. The orientation of the interface, characterized by the contact angle – the angle between the normal to the interface at the contact line and the normal to the solid boundary – is imposed in the contact line cell. It is important to note that a numerical specification of the contact angle affects the overall flow calculation in two ways:

(i) it defines the orientation of the interface reconstruction in cells that contain the contact line;

(ii) it influences the calculation of the surface tension term by affecting the curvature computed in cells at and near the contact line.

We now present the numerical implementation of the Generalized Navier Boundary Condition as written in (2.14). The boundary condition is applied on the solid surface with a smoothing function that takes into account the relative position along the boundary with respect to the contact line

$$\beta(\mathbf{v}_{\parallel} - \mathbf{U}_w) + (\mathbf{S}\mathbf{n}_{\partial\Omega})_{\parallel} + f\left(\frac{x}{\varepsilon}\right)\sigma(\cos\theta_{\mathrm{d}} - \cos\theta_{\mathrm{e}})\,\mathbf{n}_{\Gamma} = 0 \quad \text{on} \quad \partial\Omega, \tag{3.5}$$

with $f\left(\frac{x}{\varepsilon}\right)$ the discrete Dirac function defined as

$$f\left(\frac{x}{\varepsilon}\right) = \frac{\left(1 - \tanh^2\left(\frac{x}{\varepsilon}\right)\right)}{\varepsilon}. \tag{3.6}$$

This specific function is smooth, symmetric and preserves the area for varying ε, characteristics that are necessary for the well-posedness of the discrete boundary condition. The boundary condition can be expressed as an inhomogeneous Robin boundary condition for the parallel velocity $\mathbf{v}_{\parallel}$, as outlined above:

$$\mathbf{v}_{\parallel} + \frac{1}{\beta}(\mathbf{S}\mathbf{n}_{\partial\Omega})_{\parallel} = \mathbf{U}_w + \frac{1}{\beta}f\left(\frac{x}{\varepsilon}\right)\sigma(\cos\theta_{\mathrm{e}} - \cos\theta_{\mathrm{d}})\,\mathbf{n}_{\Gamma} \quad \text{on} \quad \partial\Omega. \tag{3.7}$$

We use the Navier boundary condition (Navier slip) that was implemented in the same framework in Fullana *et al.* (2020) and tested as a localized slip boundary condition in Lācis *et al.* (2020). The difference lies now in the space dependent right-handside of (3.7). The uncompensated Young's stress, that only acts at the contact line through the discrete Dirac function, needs to be computed at each grid point.

The numerical approach in this study stands out for its free contact angle method. Instead of setting the dynamic angle θ_{d}, we reconstruct it from the interface geometry and use it as an input parameter to calculate the right-hand side of (3.7). To reconstruct such a consistent angle from the volume fraction field, we use a Taylor expansion of the contact angle along the coordinate direction normal to the boundary (see y-axis in Fig. 3). This Taylor expansion uses the height function representation of the interface to compute the contact angle at the boundary from the inclination angle (or "apparent angle") θ_a one cell layer above and the interface curvature at this location according to the formula

$$\theta_d = \theta_a + \frac{3}{2}\Delta\frac{\kappa\sqrt{1+h_y^2}}{\sin\theta_a}. \tag{3.8}$$

Here, θ_d represents the extrapolated angle, θ_a is the apparent angle, Δ denotes the grid spacing, κ stands for curvature at the location of the apparent angle, and h_y represents the first-order derivative of the height function in the y direction (normal to the wall) computed using central differences. Figure 3 provides a schematic illustration of this extrapolation process. Once the extrapolated angle is computed, we enforce it through appropriate local modification of heights functions in the ghost layer, similar to a regular contact angle. Algorithm 1 is a concise summary of the two-step procedure to apply the CR-GNBC in the VOF framework.

3.2. *Kinematic transport of the contact angle*

We validate the free contact angle method presented in (3.8) through an analysis of the kinematic transport of the contact angle in a simplified setup. Leveraging kinematic considerations, Fricke *et al.* (2020); Fricke (2021) derived analytical solutions for the transport of the contact angle and the curvature for some specific velocity fields. To validate

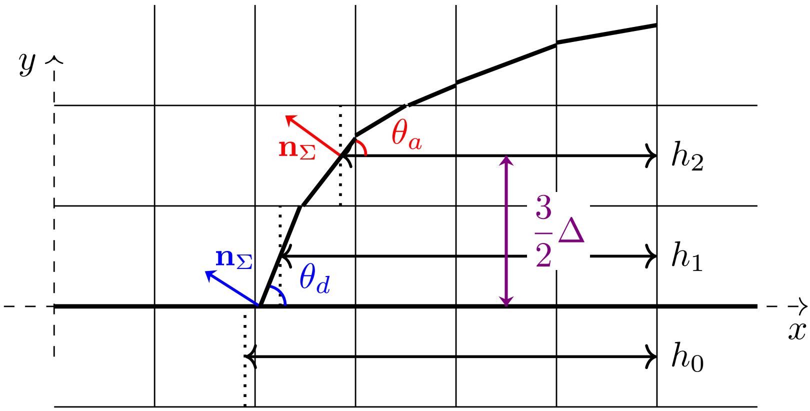

Figure 3: Extrapolation of the contact angle θ_{d} using the apparent angle θ_a located $3/2\ \Delta$ away from the wall.h_0 to h_2 denote the horizontal heights.

Algorithm 1: Free contact angle CR-GNBC pseudo-code

for *each boundary cell* **do**
1. Locate the contact line cell
2. Locate the cell one grid point above the contact line
3. Compute the apparent angle θ_a using the unit normal $\mathbf{n}_\Sigma$
4. Compute the first order derivative h_x of the height function
5. Compute the interface curvature κ
6. Compute the extrapolated angle θ_{d} using (3.8)

end

7. Apply θ_{d} at the contact line through height functions

for *each boundary cell* **do**
8. Compute the right-hand-side of (3.7) using θ_{d} and θ_{e}

end

9. Apply the boundary condition for $\mathbf{v}_{\|}$ using (3.7)

the present approach within the VOF framework, we conduct advection testcases for an initially circular interface in contact with the domain boundary. These advection tests are carried out for various grid sizes.

The setup involves a disk with a dimensionless diameter $D = 1$ in a 2×2 domain, initially placed over a static substrate with a contact angle of $\theta_0 = 90^\circ$. The velocity field across the entire domain is defined as:

$$\begin{aligned} v_x &= c_1 \cos(\pi t)\, x + c_2 \cos(\pi t)\, y, \\ v_y &= -c_1 \cos(\pi t)\, y. \end{aligned} \tag{3.9}$$

Here, v_x and v_y represent the x and y components of the velocity, while c_1 and c_2 are positive constants. We aim to validate the accuracy and reliability of the angle extrapolation method under varying grid sizes, where we only consider the advection equation of the color function (3.2).

The prescribed incompressible velocity field (3.9) will induce oscillations of the interface in both vertical and horizontal directions. The angle formed at the contact line is determined by this motion and varies in time. From the relations derived in Fricke *et al.* (2020), we

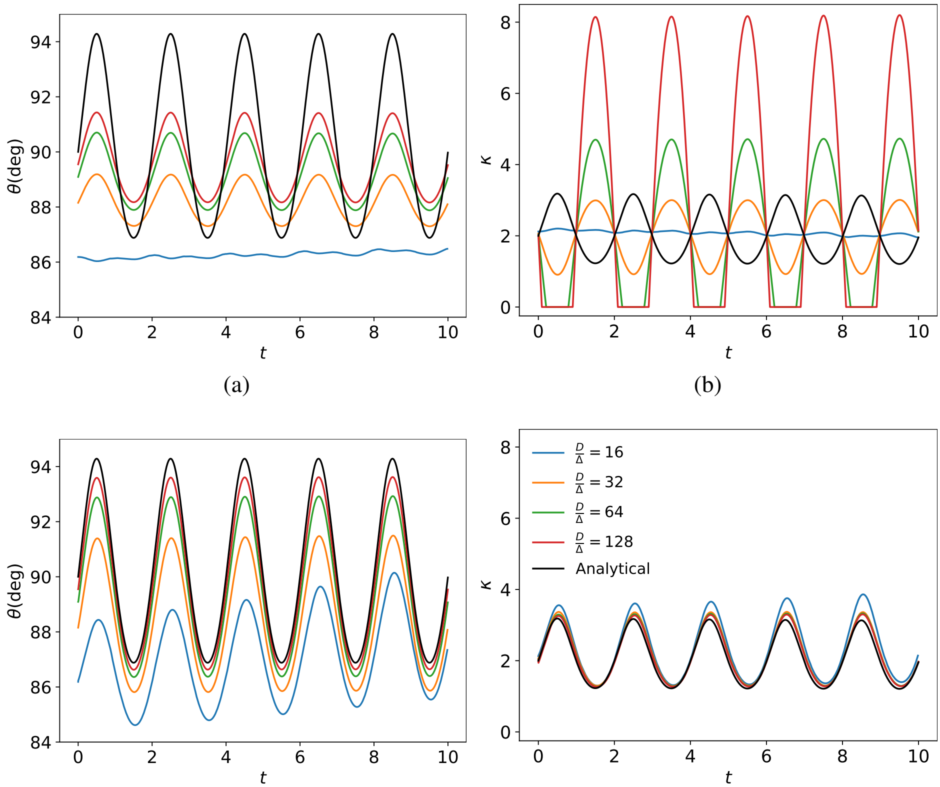

(a) (b)

(c) (d)

Figure 4: Validation of the angle extrapolation method for varying grid sizes. (a)-(b) Temporal evolution of angle and curvature for cases with a prescribed 90° contact angle. (c)-(d) Temporal evolution of angle and curvature for cases employing the extrapolated contact angle. These figures highlight divergence in the 90° case and convergence toward the analytical solution in the alternative scenario for both quantities.

compare the observed numerical contact angle with the analytical one θ_{an}, given by the formula

$$\theta_{\mathrm{an}}(t) = \frac{\pi}{2} + \tan^{-1}\left(\frac{-1}{\tan\theta_0} e^{2\,c_1\,S(t)} + \frac{c_1}{2\,c_2} e^{2\,c_1\,S(t)} - 1\right) \tag{3.10}$$

with

$$S(t) = \frac{\sin(\pi t)}{\pi}. \tag{3.11}$$

Moreover, we validate the evolution of the curvature by comparison with the reference one κ_{an}, which is given as the solution of the ordinary differential equation (see Fricke (2021))

$$\frac{d\,\kappa_{\mathrm{an}}}{dt} = -3\;\kappa_{\mathrm{an}}\;\cos(\pi t)\left[c_1\;\cos^2(\theta_{\mathrm{an}}) - c_2\;\cos(\theta_{\mathrm{an}})\sin(\theta_{\mathrm{an}}) - c_1\;\sin^2(\theta_{\mathrm{an}})\right] \tag{3.12}$$

with the initial condition $\kappa_0 = 2/D = 2$. We conduct two sets of simulations to evaluate the method. In the first set, the contact angle remains constant at 90° (corresponding to a default symmetric boundary condition for the volume fraction c), while in the second set, we enforce the extrapolated angle. The simulations run until a final dimensionless time $T = 10$, and we examine the convergence of the method with grid sizes varying from 16 to 128 points per

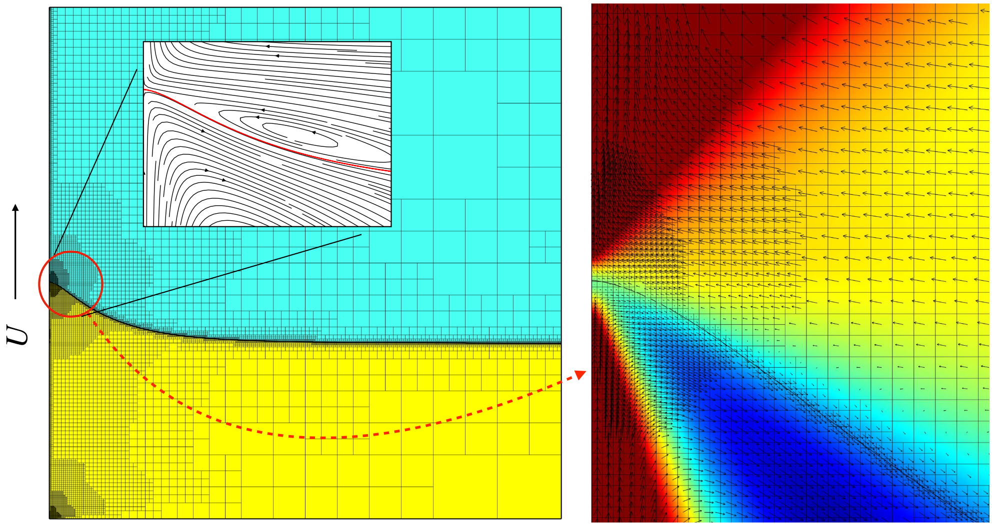

Figure 5: Steady-state meniscus example for Ca = 0.1 using the present CR-GNBC with $\varepsilon = 0.05$. The image is in the contact line's reference frame, where the left plate is pulled up with $U_w = \sqrt{\mathrm{Ca}}$. The inset, a zoomed image depicting the flow field, highlights the contact line as a stagnation point. Notably, there is an additional stagnation point in the upper phase, as indicated by the streamlines. The slip length is set equal to contact region width ε.

diameter. In Figure 4 summarizes the obtained results. The extracted contact angles show an increased accuracy and rapid convergence towards the analytical solution, thanks to the angle extrapolation method. Furthermore, the curvature is accurately transported with this method, while it diverges in the fixed at 90° contact angle case.

4. Results

We apply the numerical method for the CR-GNBC model to the pulling plate setup, following the approach discussed in Section 1. This setup is akin to the one investigated by Afkhami *et al.* (2018). Figure 5 displays the results of a steady-state simulation. The image is presented in the reference frame of the contact line, where the contact line remains stationary, while the left wall is pulled upwards. The velocity field relaxes, creating a stagnation point at the contact line. Additionally, the streamlines reveal another stagnation point formed above the interface in the lighter phase. It is worth noting that the characteristics of this additional stagnation point depend on the viscosity ratio, although our primary focus is not on this aspect.

In the pulling plate setup, a distinctive characteristic is the presence of a de-wetting transition capillary number $\mathrm{Ca}_{\mathrm{tr}}$, marking the point beyond which liquid film entrainment occurs, leading to an absence of a steady-state position for the contact line. Previous numerical results by Afkhami *et al.* (2018) identified this transition capillary number, but it was grid-dependent. Using the CR-GNBC method, with ε resolved (i.e. larger than the grid size Δ), we obtain a grid-independent $\mathrm{Ca}_{\mathrm{tr}}$. This is depicted in Figure 6, which shows the contact line position representing the fluid film height over time. For $\mathrm{Ca} \leqslant 0.12$, a steady-state height is eventually reached; however, for $\mathrm{Ca} = 0.14$, the height continually increases. Thus, we determine that $\mathrm{Ca}_{\mathrm{tr}}$ for this case is $\mathrm{Ca} = 0.13 \pm 0.01$. The influence of Young's stress is evident

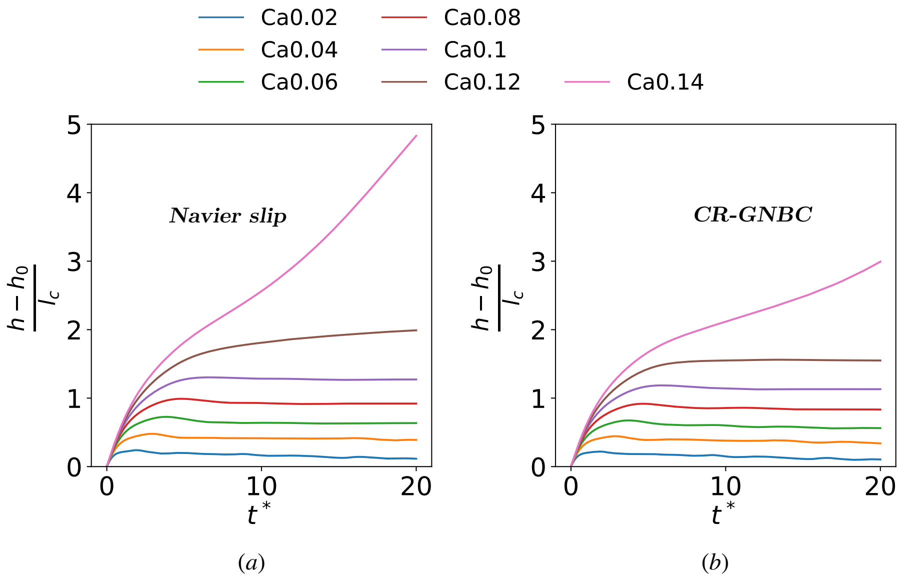

Figure 6: Vertical height of the contact line as a function of time for different capillary numbers Ca, presented separately for (a) simple Navier boundary condition and (b) CR-GNBC. Steady-state heights are achieved, and a transition $\mathrm{Ca_{tr}}$ is observed, beyond which the liquid film rises continuously. In both (a) and (b), $\mathrm{Ca_{tr}} = 0.13$. Simulations are conducted with $\varepsilon = 0.05$, $\theta_e = 90^\circ$, and a resolution of $\varepsilon/\Delta = 5.12$.

when comparing Figure 6a with Figure 6b. The $\mathrm{Ca_{tr}}$ remains the same, but the steady-state height exhibits a slight decrease. A convergence study demonstrating the grid independence of the CR-GNBC is presented in Appendix A. Furthermore, with the present approach, the parameters influencing $\mathrm{Ca_{tr}}$ are ε, the slip length λ and the equilibrium contact angle θ_e. The dependence of these parameters on the $\mathrm{Ca_{tr}}$ is presented in Appendix B.

4.1. *Relaxation towards steady state*

Starting from a horizontal two-fluid interface at rest, we now compare the transient characteristics. A distinctive feature of the present CR-GNBC model is that the contact angle is not fixed *a priori*. Figure 7a illustrates the contact angle θ_d as a function of time. The angle initiates at 90° and subsequently relaxes to a steady-state value different from 90°. Despite converging to a steady state, the observed value of θ_d exhibits spurious oscillations. These oscillations intensify with increasing Ca; however, their influence is minor, with amplitudes remaining below 0.5° and diminishing with grid refinement. In Figure7a, we observe an interesting trend when plotting θ_d against $\mathrm{Ca_{loc}}$, as shown in Figure 7b. Here, $\mathrm{Ca_{loc}}$ represents the contact line Ca in the lab frame. It starts at 0 since everything is initially at rest and eventually returns to 0 in a quasi-stationary state. During the transient phase, although we set the solid velocity to U_w instantly, $\mathrm{Ca_{loc}}$ takes some time to reach its maximum value. This time, defined as $t_\varepsilon = \varepsilon/U_w$, represents a relaxation timescale due to contact line friction. While a detailed examination of the behavior for $t < t_\varepsilon$ is beyond the current study's scope, we observe that, once $\mathrm{Ca_{loc}}$ reaches its peak, it begins to relax to the steady state where $\mathrm{Ca_{loc}} = 0$, and θ_d follows the GNBC law (2.18).

In Figure 8, we illustrate the behavior of each term of the CR-GNBC equation (3.7). We analyze and present each outcome for three different boundary conditions:

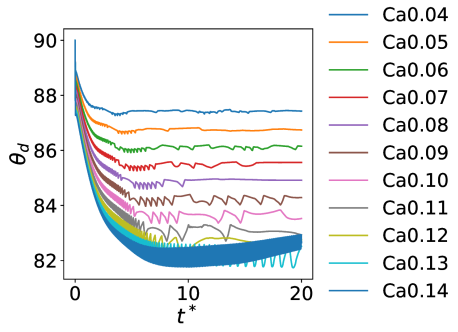

(a)

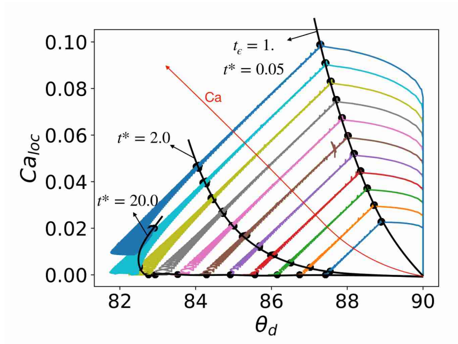

(b)

Figure 7: (a) Evolution of the dynamic contact angle θ_d in the CR-GNBC simulation for various Ca. The angle begins to deviate from the initial value of 90° and eventually reaches a steady state. Around Ca_tr, the angle exhibits oscillations over time. (b) The relaxation plot on a $\theta - \mathrm{Ca}$ plane. Here, Ca_loc represents the contact line capillary number. Time progresses from right to left, and a maximum in Ca_loc is reached at $t_\varepsilon = 1$, which corresponds to the slip length timescale (ε/U_w). After this point, Ca_loc starts relaxing towards a steady state ($\mathrm{Ca}_\mathrm{loc} = 0$). Above Ca_tr, Ca_loc reaches a minimum and starts rising again. This set of simulations are the same as in Figure 6b.

(i) Navier slip with a constant contact angle $\theta_\mathrm{d} = \theta_\mathrm{e}$:

$$\mathbf{v}_\parallel + \frac{1}{\beta}(\mathbf{S}\mathbf{n}_{\partial\Omega})_\parallel = \mathbf{U}_w \quad \text{on} \quad \partial\Omega, \tag{4.1}$$

(ii) No slip with uncompensated Young stress, with the "free angle" method (3.8):

$$\mathbf{v}_\parallel = \mathbf{U}_w + \frac{1}{\beta} f\left(\frac{x}{\varepsilon}\right) \sigma(\cos\theta_\mathrm{e} - \cos\theta_\mathrm{d})\,\mathbf{n}_\Gamma \quad \text{on} \quad \partial\Omega, \tag{4.2}$$

(iii) Full CR-GNBC as written in (3.7) which combines contributions from both the above cases.

We conducted simulations for each individual case (i), (ii), and (iii) and illustrate the behavior of each term in Figure 8. In Figure 8a we see the angle as a function of time. Since we start from a horizontal surface, all plots begin at 90°. The green curves, representing the Navier slip case, converge to the constant imposed value of 90°. The relaxation to a steady-state angle is accompanied by oscillations, whose amplitude decreases with grid refinement. The blue curves, representing the behavior of uncompensated Young's stress with a no-slip boundary condition, show the effect of the free contact angle. Because the Young stress term involves the free contact angle method, the steady-state angle differs from 90° and relaxes to the GNBC law contact angle as the grid is refined. These spurious oscillations are less pronounced than in the Navier slip case. Finally, the red curves represent the full CR-GNBC model. At the same level of grid refinement, the CR-GNBC model outperforms the Young stress case (blue curves) by being closer to the expected GNBC law contact angle and outperforms the Navier slip (green curves) by having fewer spurious oscillations. In the plot of Ca_loc vs time, we see that, although all the curves eventually relax to the steady state of $\mathrm{Ca}_\mathrm{loc} = 0$, there is a difference in the initial relaxing stage. As soon as the simulation is started we see that since blue curves have no slip, they rise to the $\mathrm{Ca}_\mathrm{loc} = \mathrm{Ca}$ in dimensionless time t_ε and then relax to the steady state value, while the CR-GNBC and slip cases rise to the value equal to $\mathrm{Ca}_\mathrm{loc} < \mathrm{Ca}$.

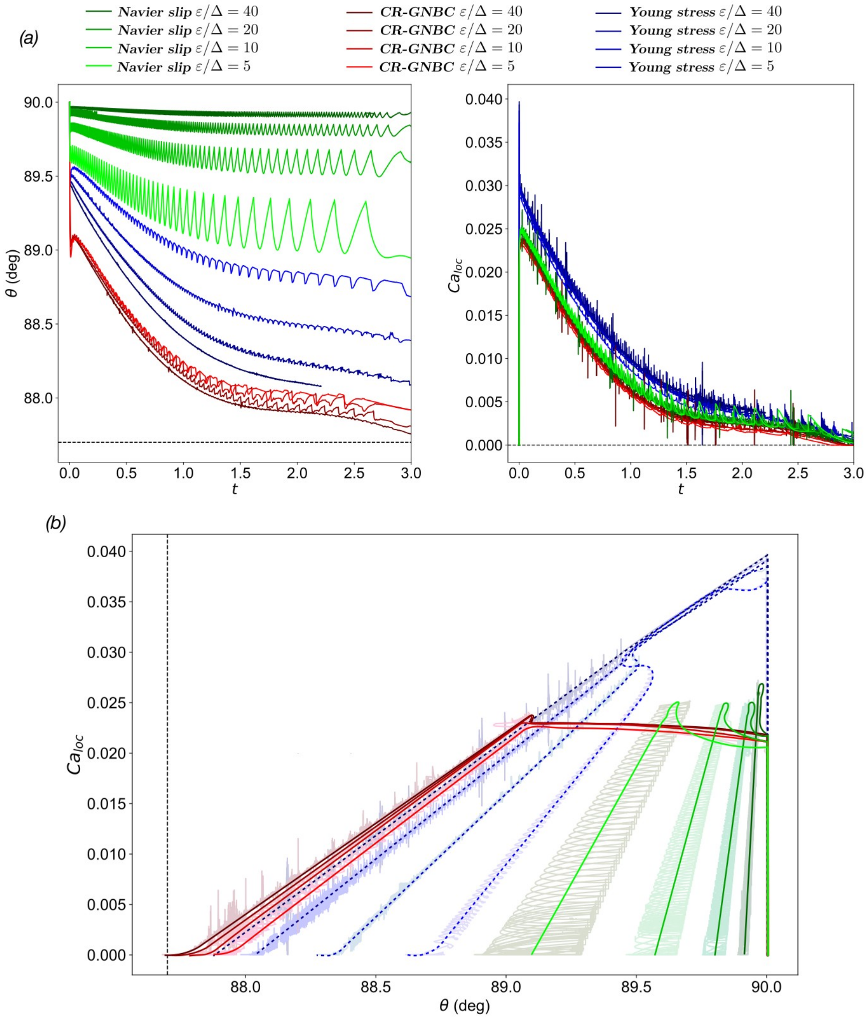

Figure 8: The relaxation plots Navier slip (green curves), CR-GNBC (red curves) and no-slip with Young stress (blue curves). All the plots are done for Ca = 0.04 and $\varepsilon = 0.05$. The grid resolution is reported in terms of ε/Δ, and color intensity is increased to show higher resolution. Figure (a) shows the contact angle θ_d and the contact line speed in the lab frame of reference $\mathrm{Ca_{loc}}$ as a function of time. In (b) we show the phase diagram resulting from figure (a). The dashed black line represents the GNBC law angle in the steady state. Time flows from right to left and aligns the curves. Each curve set has its own characteristic feature. The oscillations, present in (a), are faded in the phase diagram for clarity.

Figure 8b shows the phase diagram on a $\mathrm{Ca_{loc}} - \theta$ plane. This figure sums up the the overall behaviour of the contact line dynamics in each case and a characteristic behaviour of each set could now be identified. The timeline in this figure progresses from right to left.

(i) In the Navier slip case, we observe that at $t = 0$ and for $\theta_d = 90^{\circ}$, when the interface is horizontal, $\mathrm{Ca_{loc}}$ is null. Then, $\mathrm{Ca_{loc}}$ suddenly rises to a maximum value, which remains lower than the imposed Ca. This rapid rise occurs within the relaxation time t_{ε}, where ε is the slip length. This behavior aligns with the discussion in Figure 7b. Subsequently, the contact line relaxes to a steady state where $\mathrm{Ca_{loc}}$ returns to zero. This relaxation is accompanied by

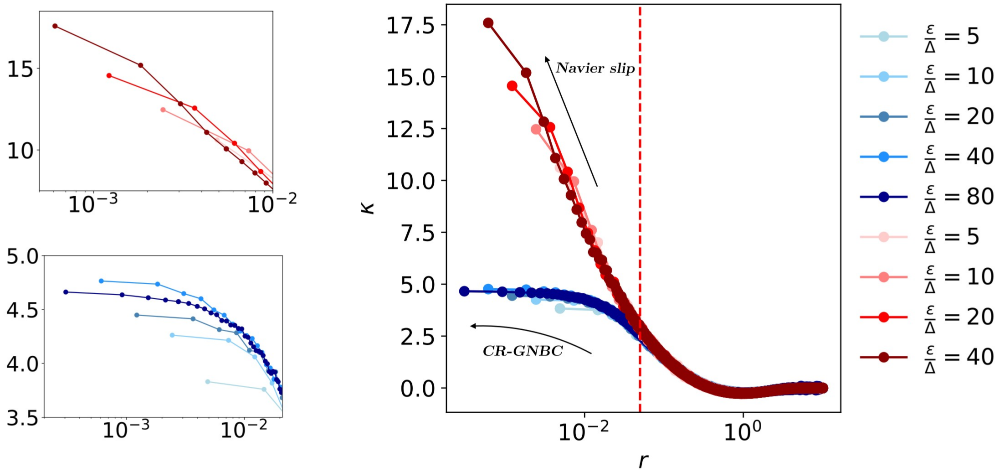

Figure 9: Curvature profiles relative to the radial distance from the contact line. The red curves represent curvature under the Navier slip boundary condition (slip), showing a logarithmic divergence. In contrast, the blue curves (GNBC), demonstrate the convergence to a finite curvature value and thus, the removal the singularity present in the NBC. Simulations are conducted with Ca = 0.08 and $\varepsilon = 0.05$. The equilibrium angle is $\theta_e = 90^{\circ}$, and Δ denotes the grid size. Various color intensities denote grid refinement, where lighter shades correspond to a coarse mesh, and darker shades indicate a fine mesh.

spurious oscillations in the contact angle θ_d. Ideally, in this case, the system should relax to $\theta_d = 90^{\circ}$ throughout the motion and also in the steady state (given that we impose a constant $\theta_d = \theta_e = 90^{\circ}$), which is indeed observed as the grid is refined. The final angle θ_d converges to 90°, and spurious oscillations diminish with increasing grid refinement.

(ii) In the no-slip with Young's stress, we notice an interesting pattern. At the start (t=0), the simulation begins with $\mathrm{Ca}_{\mathrm{loc}} = 0$ and $\theta_d = 90^{\circ}$ at the lower right of Figure 8. However, as soon as we advance in time, $\mathrm{Ca}_{\mathrm{loc}}$ increases to a maximum value equal to Ca, subsequently, starts relaxing to 0. With the presence of uncompensated Young stress, it ideally should relax to the GNBC law contact angle indicated by the dashed line in Figure 8. We observe that oscillations are decreasing with grid refinement and the final value of the contact angle is converging towards the GNBC law angle.

(iii) In the CR-GNBC case, we observe characteristics from both (i) and (ii). Initially, both $\mathrm{Ca}_{\mathrm{loc}}$ and θ_d start from zero. Subsequently, $\mathrm{Ca}_{\mathrm{loc}}$ reaches a maximum during the relaxation time and eventually relaxes to the GNBC law contact angle. The notable advantage of the CR-GNBC is that even with a modest resolution of 5 grid points per slip length, the spurious oscillations, compared to case (i) at the same resolution, are significantly reduced. Moreover, the accuracy in relaxing towards the GNBC law contact angle (dashed line) is substantially improved compared to case (ii). Further grid refinement leads to a continued reduction in spurious oscillations and enhances accuracy.

4.2. *Steady-state contact line dynamics: the GNBC smoothing signature*

We now demonstrate the full regularization of the contact line singularity achieved by the present CR-GNBC method. Figure 9 presents the curvature as a function of the distance from the contact line for various grid resolutions. The Navier slip model exhibits a logarithmic divergence in curvature, consistent with the analytical findings of Devauchelle *et al.* (2007) and Kulkarni *et al.* (2023). While the singularity in the Navier slip model is integrable and

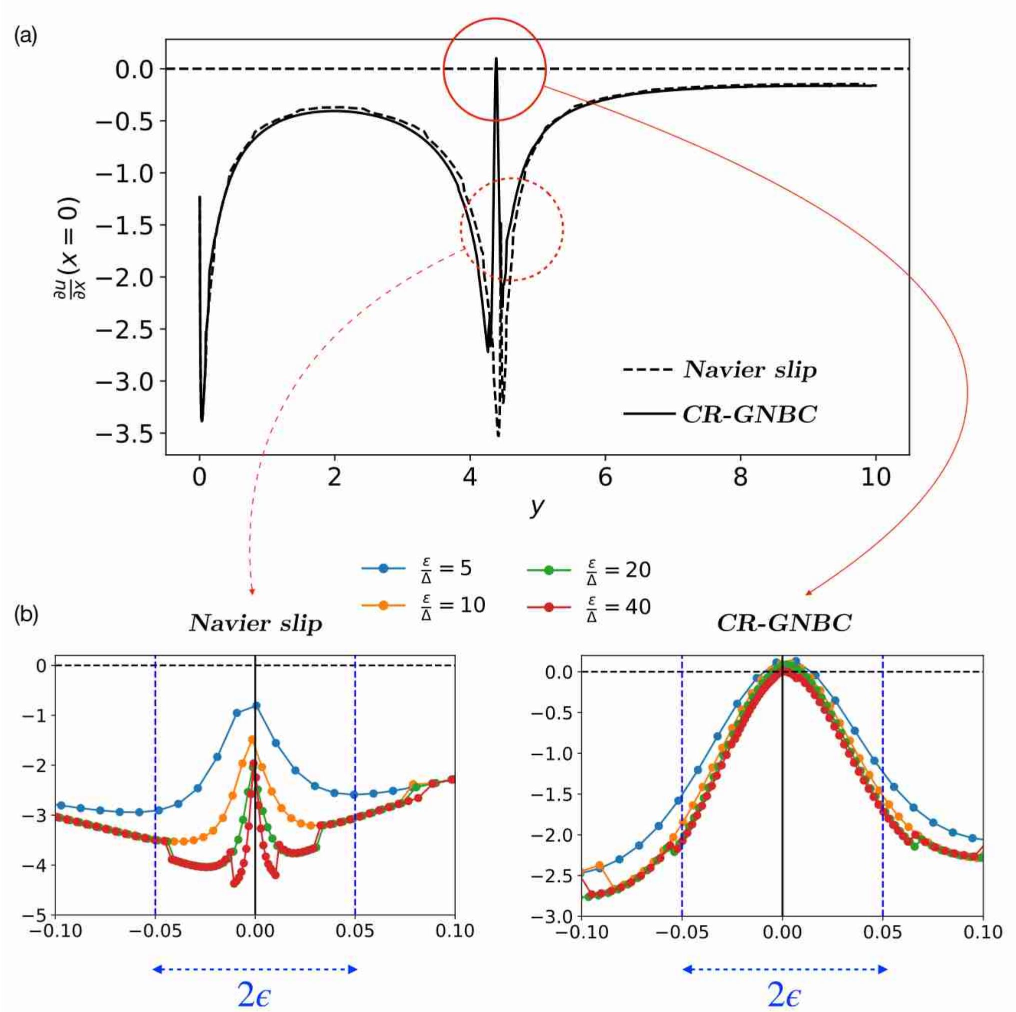

Figure 10: (a) Wall shear stress in a steady-state simulation plotted against the vertical position y. The dashed line corresponds to the Navier slip boundary condition, while the solid line corresponds to the CR-GNBC case. Both curves largely overlap, except for a small region shown in the zoom-ins for Navier slip and CR-GNBC in (b). The zoomed-in figures are normalized by the contact line position, where 0 on the x-axis corresponds to the contact line position. Notably, in the CR-GNBC case, the shear stress at the contact line is zero, whereas it is not the case for the Navier slip. The simulations are conducted with fixed Ca = 0.08 and $\varepsilon = 0.05$ and varying grid sizes.

considered “weak”, it induces a pressure singularity, rendering the slip model physically ill-posed. In contrast, the present CR-GNBC model regularizes the logarithmically singular curvature at the contact line ($\kappa \sim \log r$), establishing it as a physically well-posed model.

In Section 2, we showed that assuming a C^1 velocity field up to the contact line in the reference frame of the moving wall, the rate of change of the contact angle scales with the shear stress at the contact line. In steady state, where $\dot{\theta}_{\mathrm{d}} = 0$, the shear stress must approach zero as it reaches the contact line. A non-zero shear stress would indicate a violation of the smoothness assumption made by Fricke *et al.* (2019). This violation occurs in the Navier slip model, as non-zero shear stress is necessary for contact line motion. In Figure 10, we

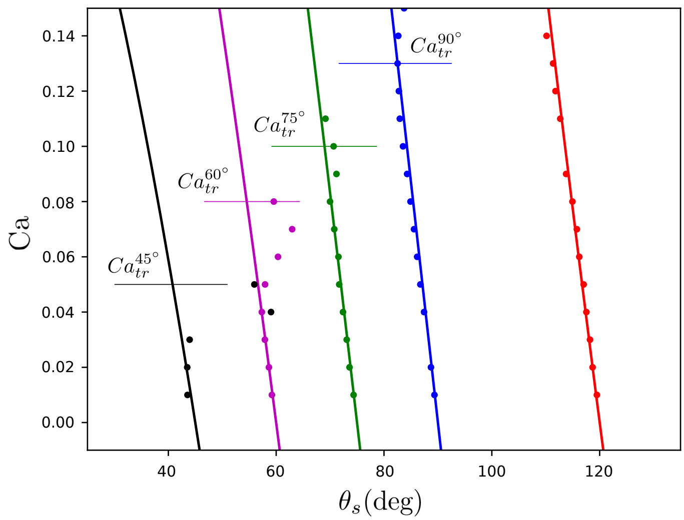

Figure 11: The behavior of the quasi-stationary value of θ_d vs Ca is illustrated for various θ_e and compared with the GNBC law (2.18). The solid lines represent the analytical expression of the steady-state behavior expected from (2.18), while the dots depict simulation results. The different colors represent various θ_e, progressing from left to right (black to red) as 45°, 60°, 75°, 90°, and 120°, respectively. The horizontal lines denote the Ca_tr for each equilibrium angle considered. An excellent agreement between simulations and the GNBC law is observed up to $Ca < \mathrm{Ca}_\mathrm{tr}$.

observe the behavior of shear stress for both Navier slip and CR-GNBC in steady state. At the contact line, the shear stress converges to zero within the ε region in the CR-GNBC case, aligning with the expected smoothness of the flow field. However, for the Navier slip model, the shear stress fails to converge to zero.

Having demonstrated that the shear stress at the contact line in the steady state is zero using the CR-GNBC, we proceed to compare the quasi-stationary state GNBC relation (2.18) with our simulation results in Figure 11. Remarkably, we observe excellent agreement between the simulation outcomes and the quasi-stationary GNBC law, particularly for $\mathrm{Ca} < \mathrm{Ca}_\mathrm{tr}$. It is essential to note that the behavior of $\mathrm{Ca}_\mathrm{cl} = f(\theta_\mathrm{s})$ in Figure 11, as predicted by the quasi-stationary GNBC law (2.15), is not explicitly imposed but is a direct outcome from the simulations.

4.3. *Asymptotic matching to the Cox region*

The smoothing is observed only within the $r < \varepsilon$ region, indicating that the outer region solution and intermediate asymptotics remain consistent with those well-known in the literature (Afkhami *et al.* 2018). Cox (1986*a*) performed an asymptotic expansion in powers of Ca and demonstrated that for any slip-like model, there exists an intermediate scale where the interface bending follows the Cox-law:

$$G(\theta_\mathrm{d}) - G(\theta(r)) = -\mathrm{Ca}\log\frac{r}{\lambda} + \mathrm{Ca}\,\frac{a_0}{f(\theta_\mathrm{d},\chi)} + O(\mathrm{Ca}^2). \tag{4.3}$$

In this equation, $G(\theta)$ is the Cox function which can be approximated as $G(\theta) = \theta^3/9$. Here, θ_d is the contact angle and $\theta(r)$ is the local angle measured at a distance r from the contact line. Other parameters include the slip length λ such that the inner region physics is captured only inside $r < \lambda$. Furthermore, χ is the viscosity ratio and a_0 is a constant obtained by

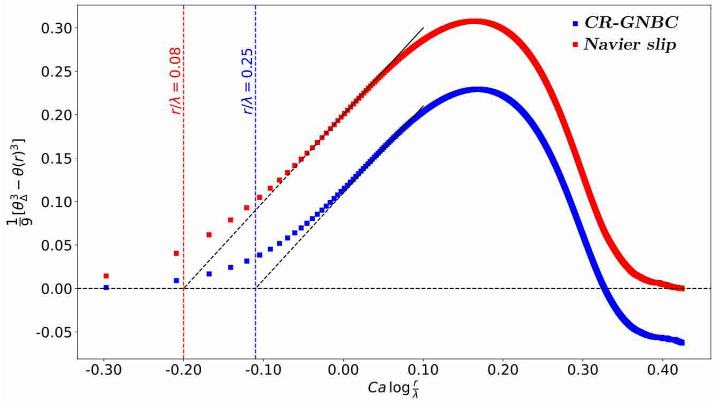

Figure 12: The Cox law matching to the inner region for CR-GNBC and Navier slip. The Cox solution becomes comparable to the inner region at a certain scale $r = c\lambda$. The value of c is 0.08 for the Navier slip and 0.25 for the CR-GNBC. The higher value of c indicates a stronger influence from the inner region. The simulations are conducted for Ca = 0.08 and $\varepsilon = \lambda = 0.05$ with 20 grid points per slip length.

matching to the outer solution. Afkhami *et al.* (2018) verified the above law and presented a wetting theory derived from the numerics with the Cox law (4.3) written as

$$G(\theta_{\mathrm{d}}) - G(\theta(r)) = \mathrm{Ca}\log(r/\ell_{mic}) + \Phi, \tag{4.4}$$

where ℓ_{mic} is the microscopic length scale equal to the grid size Δ in their work, corresponding to λ in the current work. In (4.4), Φ is a gauge function which would be obtained numerically. For further details, the reader is referred to the original work of Cox (1986*a*) and the numerical work by Afkhami *et al.* (2018).

We verify the existence of the region predicted by equation (4.4) in Appendix C. Based on the asymptotic matching section presented in the work by Kulkarni *et al.* (2023), an intermediate region exists, where the Cox solution and the inner region solution are of similar order. The Cox law in theory gives us a family of curves in the intermediate region. The final curve is then determined by matching the family to the inner region. In the present case, this means that the matching happens at $r = c\lambda$ where c depends on whether we use the Navier boundary condition or the CR-GNBC. A smaller value of Φ implies that the CR-GNBC smoothing influence region is stronger than the Navier slip one, that is $c^{\mathrm{gnbc}} > c^{\mathrm{slip}}$. This is explicitly shown in Figure 12. We can identify the following two regions, (a) an inner region present at $r \ll c\lambda$ and (b) an intermediate region $r \gg c\lambda$ where we see the interface bending. The matching happens when the two regions are of similar order at $r = c\lambda$.

5. Conclusion

To summarize, we have developed an implementation of the Contact Region Generalized Navier Boundary Condition (CR-GNBC) in a geometrical Volume-of-Fluid method. In this method, the dynamic contact angle is not prescribed but is controlled by kinematics through the velocity boundary condition. This is achieved by reconstructing the contact angle at the boundary using the interface normal and the curvature one cell layer away from the boundary. We validate the resulting free contact angle method by studying the interface advection problem in the presence of a moving contact line in Section 3.2. In the present approach, the uncompensated Young stress is distributed over a characteristic width ε, that is defined independently of the mesh size. Using the kinematic evolution equation of the dynamic contact angle (1.4), we show rigorously that the solution obeys the GNBC law (2.17), if the solution has a C^1-regularity up to the contact line. Indeed, we show in Section 4 that the weak singularity at the contact line is removed in the GNBC model with finite ε. We find a mesh-converging curvature at the contact line (see Figure 9) and the numerical solution satisfies the GNBC law in a quasi-stationary state (i.e. for $\dot{\theta}_{\mathrm{d}} = 0$). These results are consistent with the recent findings of Kulkarni *et al.* (2023) who demonstrated that this model indeed shows a local C^2-regularity at the contact line. As expected from kinematics, the tangential stress component goes to zero at the contact line in quasi-stationary states (see Figure 10). In this sense, we observe perfect apparent slip at the moving contact line. A natural follow-up of this work would be to extend the CR-GNBC to non-flat surfaces.

We now discuss in detail the implications and scope of the specific developments achieved in this paper.

1. *Development of the free contact angle method*
We have developed a method that allows us to transport the contact angle in a kinematically consistent manner. This is a major difference to the traditional approaches of imposing constant contact angle or an angle based on a mobility law. A mobility law relates the contact angle with the contact line velocity and other fluid properties like the viscosity ratio, surface tension, surface roughness etc. Vast literature already exists on many of such mobility laws (Xia & Steen 2018; Snoeijer & Andreotti 2013*b*; Ludwicki *et al.* 2022). In steady-state wetting, where the contact angle remains constant over time, there is a natural inclination to impose a constant contact angle. At this stage, we have made the hypothesis that a constant contact angle exists at nanoscopic scales in steady-state wetting processes. The next question that arises is how to determine the value of this contact angle. Typically, this is decided by solving the Stokes flow equation while assuming a constant contact angle and predicting the interface shape as a function of the capillary number, capillary length, and the contact angle. Several well-known relations exist, such as the Cox law for small angles (Cox 1986*b*; Voinov 1977) and the generalized Cox-Voinov law with the slip boundary condition of Chan *et al.* (2020). Mathematically, a simple mobility law is written as $U_{CL} = f(\theta)$, or in an inverse form $\theta = g(U_{CL})$. However, one could define generalized mobility laws such that $U_{CL} = f(\theta, \dot{\theta}, \ddot{\theta}, ...)$, or in an inverse form $\theta = g(U_{CL}, \dfrac{\partial u}{\partial y}, \dfrac{\partial^2 u}{\partial y^2}, ...)$. Note that the generalized version of the second one involves the gradients of the velocity field at the contact line which would in turn include the outer scales. We interpret the CR-GNBC in section 2.3 as one kind of generalized mobility law. Note that unlike with a simple mobility law, we cannot impose a contact angle directly based on the contact line speed. Here, our free-angle extrapolation scheme proves beneficial. Having successfully demonstrated its capability in the CR-GNBC case, future work could explore its applicability in other forms of the generalized mobility law.

2. *A grid independent contact region GNBC*
Grid independent results are obtained for a fixed ε and λ with varying grid size Δ, given that $\Delta << \varepsilon$ and $\Delta << \lambda$. We have obtained converging results even with $\varepsilon/\Delta = 5$. Obtaining grid-independent results is crucial for predicting the transition Capillary number as a function of ε and λ so that it could have a potential scope of comparison with experiments. Note that the study of Afkhami *et al.* (2018) was with no-slip boundary condition giving rise to the grid-dependent results in the Volume-of-Fluid framework. Such grid dependency is removed by using a Navier slip and resolving the slip length. We have shown that the

curvature diverges logarithmically at the contact line for the Navier slip boundary condition. A divergence in curvature implies a divergence in the pressure field making the model physically ill-posed. Unlike the non-integrable stress singularity that results from the no-slip boundary condition, the Navier slip has an integrable singularity and hence grid-independent steady-state results can be found. A logarithmic divergence of curvature is accompanied by the convergence of the contact angle this case. With the CR-GNBC, given a fixed ε, we were able to confirm the finite curvature as predicted by the thin film equation 2.5 and Kulkarni *et al.* (2023) and get a smooth flow field. A resolution as low as five grid points in the contact region was sufficient to get converged results.

3. *Shear stress and the GNBC law*
This singularity-free behaviour of CR-GNBC over the Navier slip can be seen as a result of incorporating the uncompensated Young stress. Without the uncompensated Young stress, the CR-GNBC reduces back to a classical Navier slip. From Kulkarni *et al.* (2023), we know that the Navier slip results in an only continuous velocity field at the contact line. This implies that the shear stress is mathematically not defined at the contact line. Numerical results in Figure 10b show that we have a non-converging spiked behaviour of shear stress at the contact line. From the stream-function solution of Kulkarni *et al.* (2023), we can show that the shear stress remains bounded up to the contact line while the differentiability for the shear stress is lost at the contact line. We also observe, from Figure 10, that once uncompensated Young stress is added, the shear stress at the contact line goes to zero in a converging and smooth manner. The GNBC law that relates the steady state value for the contact angle and the velocity of the contact line as one would expect in the vanishing shear stress limit. This is perfectly in-line with requirement for a smooth flow from Fricke *et al.* (2018, 2019). Notably, this smooth behaviour of shear stress going to zero in the CR-GNBC happens only within the ε width, i.e. within the contact region. In the derivation of the GNBC from entropy principles (Fricke *et al.* 2020), we introduced a smoothed uncompensated Young stress as a Dirac function. This smoothed region can be seen as a physical contact region. However, for mathematical coupling of terms, it remains to be seen how the shear stress would behave if we retained a delta function GNBC formulation. That is, considering an uncompensated Young stress in the singular form of a true delta function, and how it would interact with the singularity of the Navier slip. An investigation of this case is left as a future task.

4. *The Cox law asymptotics*
We have shown in Section 4.3 that with the CR-GNBC, we observe the slip-like Cox law at an intermediate scale $\varepsilon < r < l_c$, where l_c is the capillary length. This suggests that CR-GNBC primarily smoothens the contact region solution ($r \ll \varepsilon$), while preserving the appropriate solution at intermediate and outer scales. Our setup involves a receding contact line scenario with Ca $\ll 1$, allowing validation against the Cox law. However, it remains to be investigated how CR-GNBC would impact dynamic wetting systems with an advancing contact line where Ca $\sim \mathcal{O}(1)$. It is important to note that the physical speed in the advancing contact line setup can result in a Ca value that exceeds the range of the linear GNBC law. Section 6 is dedicated to this outlook of the non-linear GNBC whose numerical implementation is left as a future scope.

5. *Extension to transient regime*
In the paper we have dealt with the steady-state flow characteristics of the GNBC. The work should now be extended to incorporate the setups that have a transient contact line behaviour. Examples of such setups include nano-scale shear droplet (Lācis *et al.* 2022) and a spreading

drop. Mohammad Karim *et al.* (2016) showed that despite using the same fluids and solid material, the overall configuration of the system can result in different values of the apparent contact angle even for equal contact line speeds. The forced wetting case of a plunging plate exhibited a different apparent angle than the spontaneous wetting case of a spreading drop, even when the contact line speed is equal to the plate velocity. Thus a simple mobility law cannot capture this dependence. However, the GNBC contains a term representing the rate of change of the contact angle 2.17 which makes spontaneous wetting different from the forced wetting and whether CR-GNBC could explain the experimental behaviour remains an unanswered question. The CR-GNBC should also be extended to setups having sustained oscillatory states. The vibrating drop is a famous example of this setup Xia & Steen (2018). There have been several models to describe such oscillatory setups, but most of them rely on empirical relations (Kistler 1993). Sakakeeny & Ling (2021) numerically predicted the first and second modal frequencies of a vibrating droplet in two limiting cases (a) a pinned contact line and (b) a free-slip contact line. In reality, the contact line is expected to behave in between these two limits. Whether a fundamental boundary condition like the CR-GNBC could recover the modal frequencies on large scale as well as the contact line hysteresis at micrometre scale as observed by Xia & Steen (2018), remains to be tested.

6. Outlook: A non-linear generalization of the GNBC

As discussed in detail in Section 2.2, the CR-GNBC in the form

$$-\beta(\mathbf{v}_{\|} - \mathbf{U}_w) = (\mathbf{S}\mathbf{n}_{\partial\Omega})_{\|} + \sigma(\cos\theta_{\mathrm{d}} - \cos\theta_{\mathrm{e}})\,\mathbf{n}_\Gamma \delta_\Gamma^\varepsilon \quad \text{on} \quad \partial\Omega \tag{6.1}$$

is obtained as a *linear* closure relation, to render the dissipation integral

$$\mathcal{T} = \int_{\partial\Omega} \left((\mathbf{S}\mathbf{n}_{\partial\Omega})_{\|} + \sigma(\cos\theta_{\mathrm{d}} - \cos\theta_{\mathrm{e}})\,\mathbf{n}_\Gamma \delta_\Gamma^\varepsilon \right) \cdot (\mathbf{v}_{\|} - \mathbf{U}_w)\, dA \tag{6.2}$$

non-positive. Since, according to kinematics, the viscous stress contribution vanishes in a quasi-stationary state (see Section 2), we obtain the dynamic contact angle relation

$$-\zeta U_{\mathrm{cl}} = \sigma(\cos\theta_{\mathrm{d}} - \cos\theta_{\mathrm{e}}) \tag{6.3}$$

with the contact line friction coefficient $\zeta = \beta\varepsilon$. Notably, equation (6.3) is also found in the Molecular Kinetic Theory (MKT) in the limit of low capillary number (see, e.g., Blake *et al.* (2015)). However, for higher capillary numbers, the MKT predicts that†

$$U_{\mathrm{cl}} = 2\kappa^0 \Lambda \sinh\left[\sigma\left(\cos\theta_{\mathrm{e}} - \cos\theta_{\mathrm{d}}\right)/(2nk_B T)\right]. \tag{6.4}$$

Therefore, it is interesting to formulate a closure relation for (6.2) that will lead to the relation (6.4) in quasi-stationary states. Notice that (6.4) can be linearized for $U_{\mathrm{cl}} \to 0$ using $\sinh(x) = x + O(x^3)$. Hence, the contact line friction coefficient is identified as $\zeta = (nk_B T)/(\kappa^0 \Lambda)$.

For simplicity, let us assume that $\mathbf{U}_w = 0$ in the following (the generalization to $\mathbf{U}_w \neq 0$ is obvious). To proceed, it is useful to decompose the integral in (6.2) into its components normal and tangential to the contact line, according to

$$\mathbf{v}_{\|} = (\mathbf{v}_{\|} \cdot \mathbf{n}_\Gamma)\,\mathbf{n}_\Gamma + (\mathbf{v}_{\|} \cdot \mathbf{t}_\Gamma)\,\mathbf{t}_\Gamma.$$

† In this case, the average distance and equilibrium frequency of molecular jumps are denoted by Λ and κ^0, respectively. Moreover, n is the number of adsorption sites per unit area, k_B is the Boltzmann constant and T is the absolute temperature; see Blake *et al.* (2015) for more details.

Here, we denote by $\mathbf{t}_\Gamma$ the tangent vector to the contact line. We obtain the representation

$$\mathcal{T} = \mathcal{T}_\perp + \mathcal{T}_\parallel \tag{6.5}$$

with

$$\mathcal{T}_\parallel = \int_{\partial\Omega} \left(\mathbf{t}_\Gamma \cdot (\mathbf{S}\mathbf{n}_{\partial\Omega})_\parallel\right) \left(\mathbf{t}_\Gamma \cdot \mathbf{v}_\parallel\right) dA$$

and

$$\mathcal{T}_\perp = \int_{\partial\Omega} \left(\mathbf{n}_\Gamma \cdot (\mathbf{S}\mathbf{n}_{\partial\Omega})_\parallel + \sigma(\cos\theta_{\mathrm{d}} - \cos\theta_{\mathrm{e}})\,\delta_\Gamma^\varepsilon\right) \left(\mathbf{n}_\Gamma \cdot \mathbf{v}_\parallel\right) dA. \tag{6.6}$$

We are now looking for closure relations to ensure that $\mathcal{T}_\perp \leqslant 0$ and $\mathcal{T}_\parallel \leqslant 0$. A general non-linear closure for $\mathcal{T}_\perp$ reads as

$$\boxed{\mathbf{n}_\Gamma \cdot (\mathbf{S}\mathbf{n}_{\partial\Omega})_\parallel + \sigma(\cos\theta_{\mathrm{d}} - \cos\theta_{\mathrm{e}})\,\delta_\Gamma^\varepsilon = -f(\mathbf{n}_\Gamma \cdot \mathbf{v}_\parallel),} \tag{6.7}$$

where the scalar function f satisfies the inequality

$$x f(x) \geqslant 0 \quad \forall x \in \mathbb{R}.$$

Such a closure is consistent with the second law of thermodynamics because it implies that

$$\mathcal{T}_\perp = -\int_{\partial\Omega} (\mathbf{n}_\Gamma \cdot \mathbf{v}_\parallel) f(\mathbf{n}_\Gamma \cdot \mathbf{v}_\parallel) \leqslant 0.$$

The linear version of the GNBC is recovered as $f(x) = \beta x$. Motivated by (6.4), a special choice is

$$f(x) = b \operatorname{arcsinh}(x/a). \tag{6.8}$$

with positive constants $a = 2\kappa^0\Lambda$ and $b = 2nk_BT$. Clearly, Equation (6.8) reduces by linearization to the original GNBC (6.1) with $\beta = b/a$ if $\mathbf{v}_\parallel \cdot \mathbf{n}_\Gamma \longrightarrow 0$. Since (6.8) corresponds to the MKT (6.4) for quasi-stationary states, it may improve the standard GNBC model for higher values of the capillary number. This shall be studied in detail in the future.

Author contributions.. TF, YK and MF contributed equally to this work that includes free angle method, performing simulations and writing paper with feedback from all authors. Study was performed at all three institutes hosted by SA, DB and SZ. Detailed discussions were done among all authors on all the ideas presented in the paper.

Funding.. This project has received funding from the European Research Council (ERC) under the European Union's Horizon 2020 research and innovation programme (grant agreement n° 883849). MF and DB acknowledge the financial support by the German Research Foundation (DFG) within the Collaborative Research Centre 1194 (Project-ID 265191195).

Appendix A. Convergence study

We conduct a convergence study to demonstrate the grid independence of the CR-GNBC. In Figure 13a, we present interface shapes for a fixed Ca = 0.12 and $\varepsilon = 0.2$ with varying resolutions, showing apparent convergence. In Figure 13, we display the percentage error in the contact line position for this case, revealing second-order convergence. This confirms that unlike Afkhami *et al.* (2018) our CR-GNBC method achieves grid independence for steady-state height with a fixed Ca and ε, including the $\mathrm{Ca}_{\mathrm{tr}}$.

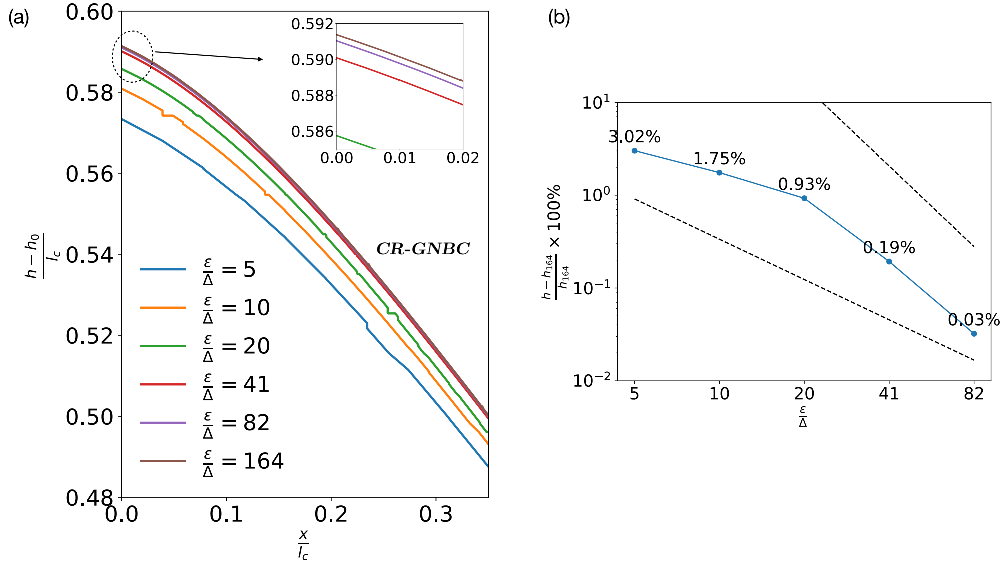

Figure 13: Steady-state height and interface shapes near the contact line with varying grid resolution for the CR-GNBC. In (a), Ca = 0.12 and $\varepsilon = 0.2$ are fixed, showing convergent interface shapes. In (b), a fixed Ca = 0.04 reveals that due to implicit slip, steady-state solutions are achievable even with a no-slip boundary condition. Interface shapes do not converge with grid refinement, and no steady-state height is found at resolutions higher than $l_c/\Delta > 100$. (b) Percentage error in the contact line position for steady-state interface shapes obtained in (a). The reference solution is taken at 164 grid points per slip length ε/Δ, and the dashed lines represent second-order and first-order convergence. It is observed that above 20 grid points per ε, a second-order convergence is achieved.

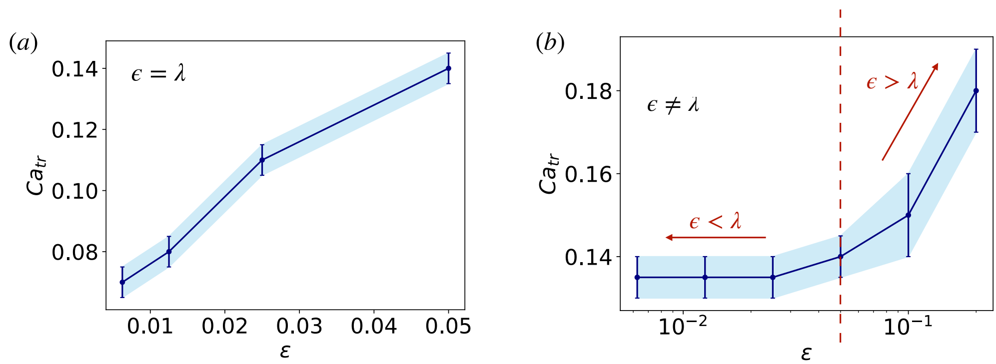

Figure 14: Transition capillary number plotted against variation of (a) ε and λ with $\varepsilon = \lambda$, and (c) ε such that the slip length λ is fixed. All simulations are carried out with the CR-GNBC and $\theta_e = 90^{\circ}$. The resolution for all simulations is maintained at $\min(\varepsilon, \lambda)/\Delta = 5.12$.

Appendix B. Transition capillary number and the contact region width ε

Figure 14 illustrates Ca_{tr} as a function of ε, λ and θ_e. When we have $\varepsilon = \lambda$, we see that Ca_{tr} decreases with the decrease of ε. When we break the restriction of $\varepsilon = \lambda$, we see an interesting behaviour in Figure 14(c). Since we know that ε and λ, both promote smoothing behaviour, the Ca_{tr} is decided by the larger of the two. Hence, when we decrease ε below the slip length λ, we see that $\mathrm{Ca}_{\mathrm{tr}}$ goes to a constant value. The dependence on the equilibrium contact angle shown in Figure 14(b) is notably linear. While this linearity may break at smaller angles, it's important to note that our solver, which employs only horizontal heights, faces limitations in handling angles smaller than 30°.

Appendix C. The Cox law and the gauge factor

Figures 15 and 16 show the existence of the Cox region. These figures show, in particular, that the gauge function in equation (4.4) for the CR-GNBC is always less than the gauge function of the Navier slip. This implies that the inner region influence of the CR-GNBC is higher than that of the Navier slip at same ε. This is perfectly in line with the fact that CR-GNBC solution is smoother than the Navier slip solution.

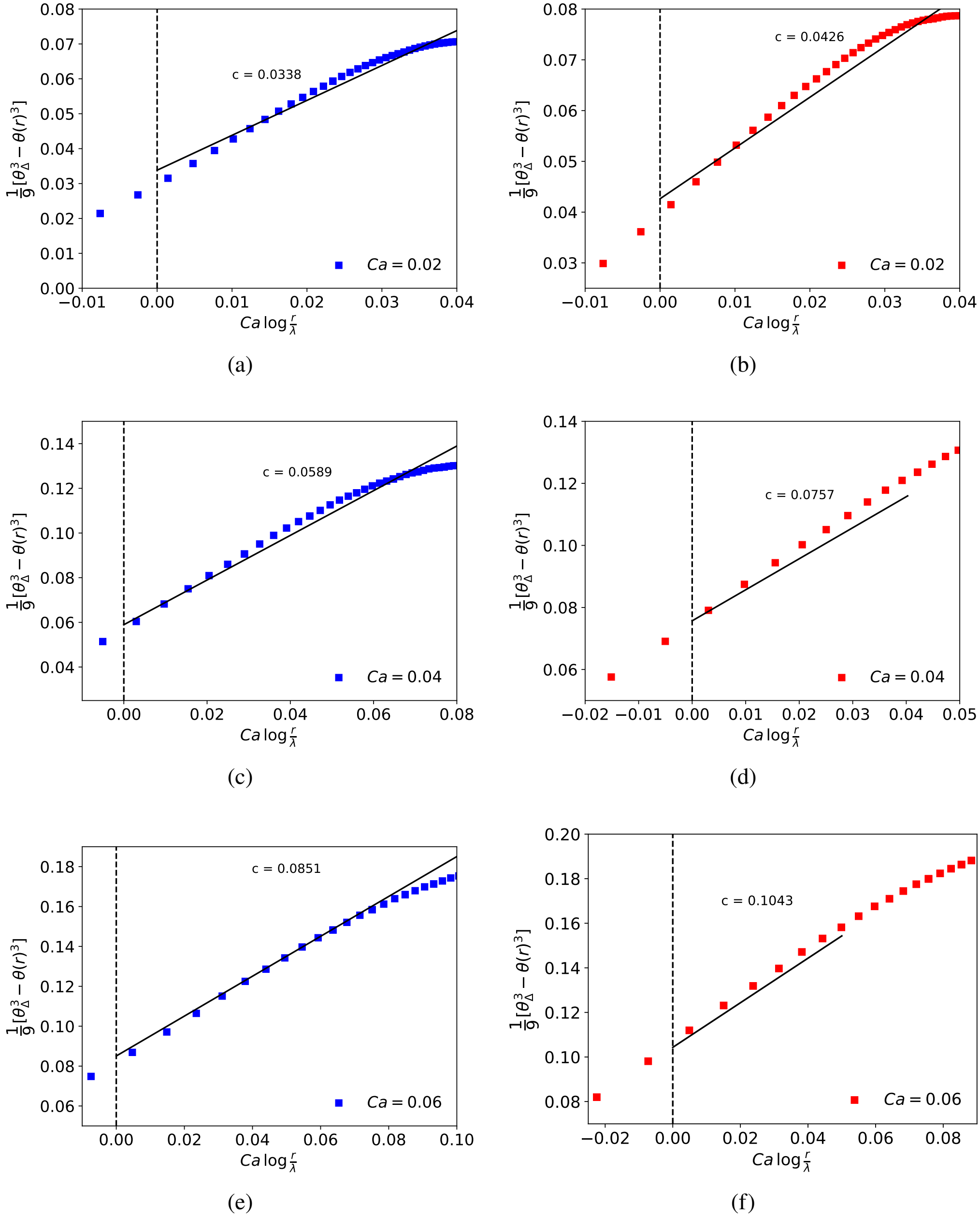

Figure 15: Comparison of the Cox law observed at an intermediate scale in our simulations for the CR-GNBC (blue) and Navier slip (red). The vertical dashed line represents the slip length λ, which is equivalent to the CR-GNBC width ε. The solid black lines follow the Cox law (4.4), approximated as ${\theta_\Delta}^3 - \theta^3(r) = 9\,\mathrm{Ca}\log(r/\lambda) + c$. Here, θ_Δ is the contact angle observed in the simulations at the contact line cell. The value of c is provided in the plot for each case, with a smaller c observed for the CR-GNBC. $\theta_e = 90^\circ$ for all simulations, resulting in a constant $\theta_\Delta = 90^\circ$ for Navier slip and $\theta_\Delta = \theta_d$ for the CR-GNBC. $\lambda = 0.05$, and the resolution is $\lambda/\Delta = 10$ in all cases.

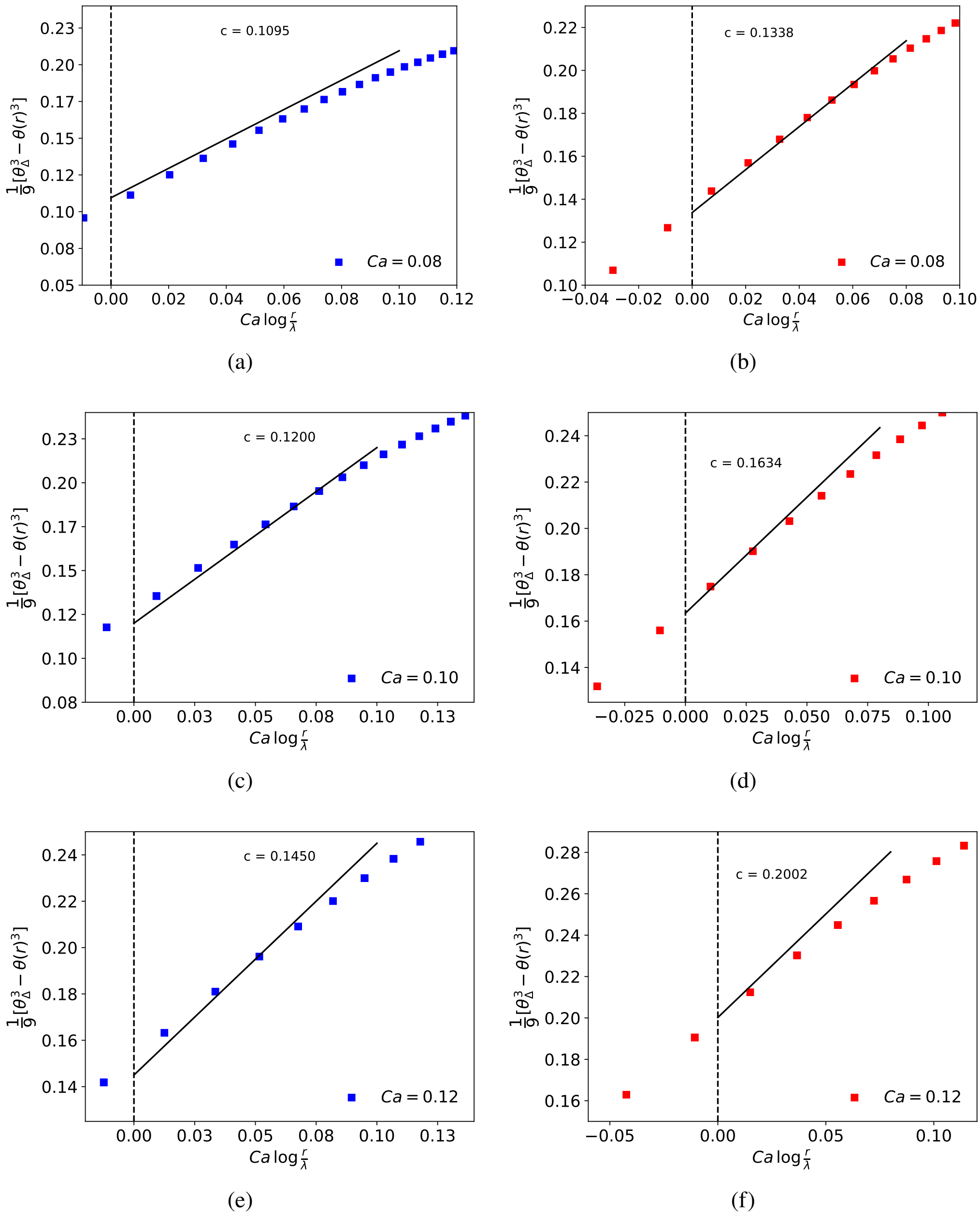

Figure 16: An extension of Figure 15 for higher values of Ca. All the other parameters are identical to those in Figure 15. The matching with the Cox law starts to deteriorate as Ca is increased, aligning with theoretical expectations.

REFERENCES

Afkhami, S., Buongiorno, J., Guion, A., Popinet, S., Saade, Y., Scardovelli, R. & Zaleski, S. 2018 Transition in a numerical model of contact line dynamics and forced dewetting. *Journal of Computational Physics* **374**, 1061–1093.

Afkhami, S. & Bussmann, M. 2008 Height functions for applying contact angles to 2D VOF simulations. *International Journal for Numerical Methods in Fluids* **57** (4), 453–472.

Afkhami, S. & Bussmann, M. 2009 Height functions for applying contact angles to 3D VOF simulations. *International Journal for Numerical Methods in Fluids* **61** (8), 827–847.

Blake, T.D & Haynes, J.M. 1969 Kinetics of liquid-liquid displacement. *Journal of Colloid and Interface Science* **30** (3), 421–423.

Blake, T. D. 2006 The physics of moving wetting lines. *Journal of Colloid and Interface Science* **299** (1), 1–13.

Blake, T. D., Fernandez-Toledano, J.-C., Doyen, G. & De Coninck, J. 2015 Forced wetting and hydrodynamic assist. *Physics of Fluids* **27** (11), 112101.

Bonn, D., Eggers, J., Indekeu, J., Meunier, J. & Rolley, E. 2009 Wetting and spreading. *Reviews of Modern Physics* **81** (2), 739–805.

Chan, Tak Shing, Kamal, Catherine, Snoeijer, Jacco H., Sprittles, James E. & Eggers, Jens 2020 Cox–voinov theory with slip. *Journal of Fluid Mechanics* **900**, A8.

Chen, Xianyang, Lu, Jiacai & Tryggvason, Grétar 2019 Numerical simulation of self-propelled non-equal sized droplets. *Physics of Fluids* **31** (5), 052107.

Cox, R. G. 1986*a* The dynamics of the spreading of liquids on a solid surface. part 1. viscous flow. *Journal of Fluid Mechanics* **168**, 169–194.

Cox, R. G. 1986*b* The dynamics of the spreading of liquids on a solid surface. Part 1. Viscous flow. *Journal of Fluid Mechanics* **168**, 169–194.

Devauchelle, O., Josserand, C. & Zaleski, S. 2007 Forced dewetting on porous media. *Journal of Fluid Mechanics* **574**, 343–364.

Duffy, Brian R. & Wilson, Stephen K. 1997 A third-order differential equation arising in thin-film flows and relevant to tanner's law. *Applied Mathematics Letters* **10**, 63–68.

Eggers, Jens 2004 Hydrodynamic theory of forced dewetting. *Phys. Rev. Lett.* **93**, 094502.

Fricke, M. 2021 Mathematical modeling and volume-of-fluid based simulation of dynamic wetting. PhD thesis, TU Darmstadt.

Fricke, M. & Bothe, D. 2020 Boundary conditions for dynamic wetting - A mathematical analysis. *The European Physical Journal Special Topics* **229** (10), 1849–1865.

Fricke, M., Köhne, M. & Bothe, D. 2019 A kinematic evolution equation for the dynamic contact angle and some consequences. *Physica D: Nonlinear Phenomena* **394**, 26–43.

Fricke, M., Köhne, M. & Bothe, D. 2018 On the kinematics of contact line motion. *PAMM* **18** (1), e201800451.

Fricke, M., Marić, T. & Bothe, D. 2020 Contact Line Advection using the geometrical Volume of Fluid Method. *Journal of Computational Physics* **407**, 109221.

Fullana, T., Zaleski, S. & Popinet, S. 2020 Dynamic wetting failure in curtain coating by the Volume-of-Fluid method. *The European Physical Journal Special Topics* **229** (10), 1923–1934.

Fumagalli, I., Parolini, N. & Verani, M. 2018 On a free-surface problem with moving contact line: From variational principles to stable numerical approximations. *Journal of Computational Physics* **355**, 253–284.

de Gennes, P.-G., Brochard-Wyart, F. & Quéré, D. 2004 *Capillarity and Wetting Phenomena*. New York, NY: Springer New York.

Gerbeau, J.-F. & Lelièvre, T. 2009 Generalized Navier boundary condition and geometric conservation law for surface tension. *Computer Methods in Applied Mechanics and Engineering* **198** (5-8), 644–656.

Hocking, L. M. 2001 Meniscus draw-up and draining. *European Journal of Applied Mathematics* **12** (3), 195–208.

Huh, C. & Mason, S. G. 1977 The steady movement of a liquid meniscus in a capillary tube. *Journal of Fluid Mechanics* **81** (03), 401–419.

Huh, C. & Scriven, L. E 1971 Hydrodynamic model of steady movement of a solid/liquid/fluid contact line. *Journal of Colloid and Interface Science* **35** (1), 85–101.

Jacqmin, David 2000 Contact-line dynamics of a diffuse fluid interface. *Journal of Fluid Mechanics* **402**, 57–88.

Kawakami, K., Kita, Y. & Yamamoto, Y. 2023 Front-tracking simulation of the wetting behavior of an impinging droplet using a relaxed impermeability condition and a generalized navier boundary condition. *Computers & Fluids* **251**, 105739.

Kistler, Stephan F 1993 Hydrodynamics of wetting. *Wettability* **6**, 311–430.

Kulkarni, Yash, Fullana, Tomas & Zaleski, Stephane 2023 Stream function solutions for some contact line boundary conditions: Navier slip, super slip and the generalized navier boundary condition. *Proceedings of the Royal Society A: Mathematical, Physical and Engineering Sciences* **479** (2278).

Ludwicki, JM, Kern, VR, McCraney, J, Bostwick, JB, Daniel, S & Steen, PH 2022 Is contact-line mobility a material parameter? npj microgravity. *NPJ Microgravity* .

Lukyanov, A. V. & Pryer, T. 2017 Hydrodynamics of moving contact lines: Macroscopic versus microscopic. *Langmuir* **33** (34), 8582–8590.

Lācis, U., Johansson, P., Fullana, T., Hess, B., Amberg, G., Bagheri, S. & Zaleski, S. 2020 Steady moving contact line of water over a no-slip substrate. *The European Physical Journal Special Topics* **229** (10), 1897–1921.

Lācis, Uğis, Pellegrino, Michele, Sundin, Johan, Amberg, Gustav, Zaleski, Stéphane, Hess, Berk & Bagheri, Shervin 2022 Nanoscale sheared droplet: volume-of-fluid, phase-field and no-slip molecular dynamics. *Journal of Fluid Mechanics* **940**, A10.

Marengo, Marco & De Coninck, Joel, ed. 2022 *The Surface Wettability Effect on Phase Change*. Springer International Publishing.

Marić, T., Kothe, D. B. & Bothe, D. 2020 Unstructured un-split geometrical Volume-of-Fluid methods – A review. *Journal of Computational Physics* **420**, 109695.

Mohammad Karim, A., Davis, S. H. & Kavehpour, H. P. 2016 Forced versus spontaneous spreading of liquids. *Langmuir* **32** (40), 10153–10158, pMID: 27643428, arXiv: https://doi.org/10.1021/acs.langmuir.6b00747.

Popinet, S. 2009 An accurate adaptive solver for surface-tension-driven interfacial flows. *Journal of Computational Physics* **228** (16), 5838–5866.

Popinet, S. 2015 A quadtree-adaptive multigrid solver for the serre–green–naghdi equations. *J. Comput. Phys.* **302**, 336–358.

Popinet, S. 2018 Numerical Models of Surface Tension. *Annual Review of Fluid Mechanics* **50** (1), 49–75.

Popinet, Stéphane & Zaleski, Stéphane 1999 A front-tracking algorithm for accurate representation of surface tension. *International Journal for Numerical Methods in Fluids* **30** (6), 775–793.

Prüss, J. & Simonett, G. 2016 *Moving interfaces and quasilinear parabolic evolution equations*. *Monographs in Mathematics* . Switzerland: Birkhäuser.

Qian, T., Wang, X.-P. & Sheng, P. 2003 Molecular scale contact line hydrodynamics of immiscible flows. *Physical Review E* **68** (1 Pt 2), 016306.

Qian, T., Wang, X.-P. & Sheng, P. 2006*a* A variational approach to moving contact line hydrodynamics. *Journal of Fluid Mechanics* **564**, 333.

Qian, T., Wang, X.-P. & Sheng, P. 2006*b* Molecular hydrodynamics of the moving contact line in two-phase immiscible flows. *Commun. Comput. Phys.* **1** (1), 1–52.

Sakakeeny, Jordan & Ling, Yue 2021 Numerical study of natural oscillations of supported drops with free and pinned contact lines. *Physics of Fluids* **33** (6), 062109, arXiv: https://pubs.aip.org/aip/pof/article-pdf/doi/10.1063/5.0049328/15909411/062109_1_online.pdf.

Scardovelli, R. & Zaleski, S. 1999 Direct Numerical Simulation of Free-Surface and Interfacial Flow. *Annual Review of Fluid Mechanics* **31** (1), 567–603.

Shang, Xinglong, Luo, Zhengyuan, Gatapova, Elizaveta Ya., Kabov, Oleg A. & Bai, Bofeng 2018 GNBC-based front-tracking method for the three-dimensional simulation of droplet motion on a solid surface. *Computers & Fluids* **172**, 181–195.

Shikhmurzaev, Y. D. 1993 The moving contact line on a smooth solid surface. *International Journal of Multiphase Flow* **19** (4), 589–610.

Shikhmurzaev, Y. D. 2006 Singularities at the moving contact line. Mathematical, physical and computational aspects. *Physica D: Nonlinear Phenomena* **217** (2), 121–133.

Shikhmurzaev, Y. D. 2008 *Capillary flows with forming interfaces*. Boca Raton: Chapman & Hall/CRC.

Slattery, J. C. 1999 *Advanced transport phenomena*. *Cambridge Series in Chemical Engineering* . Cambridge: Cambridge University Press.

Snoeijer, J. H. & Andreotti, B. 2013*a* Moving contact lines: Scales, Regimes, and Dynamical Transitions. *Annual Review of Fluid Mechanics* **45** (1), 269–292.

Snoeijer, Jacco H. & Andreotti, Bruno 2013*b* Moving contact lines: Scales, regimes, and dynamical transitions. *Annual Review of Fluid Mechanics* **45** (Volume 45, 2013), 269–292.

Thompson, Peter A. & Robbins, Mark O. 1989 Simulations of contact-line motion: Slip and the dynamic contact angle. *Physical Review Letters* **63** (7), 766–769.

Tryggvason, G., Scardovelli, R. & Zaleski, S. 2011 *Direct numerical simulations of gas-liquid multiphase flows*. Cambridge University Press.

Voinov, O. V. 1977 Hydrodynamics of wetting. *Fluid Dynamics* **11** (5), 714–721.

Xia, Yi & Steen, Paul H. 2018 Moving contact-line mobility measured. *Journal of Fluid Mechanics* **841**, 767–783.

Yamamoto, Y., Higashida, S., Tanaka, H., Wakimoto, T., Ito, T. & Katoh, K. 2016 Numerical analysis of contact line dynamics passing over a single wettable defect on a wall. *Physics of Fluids* **28** (8).

Yamamoto, Y., Ito, T., Wakimoto, T. & Katoh, K. 2013 Numerical simulations of spontaneous capillary rises with very low capillary numbers using a front-tracking method combined with generalized navier boundary condition. *International Journal of Multiphase Flow* **51**, 22–32.

Yamamoto, Y., Tokieda, K., Wakimoto, T., Ito, T. & Katoh, K. 2014 Modeling of the dynamic wetting behavior in a capillary tube considering the macroscopic–microscopic contact angle relation and generalized navier boundary condition. *International Journal of Multiphase Flow* **59**, 106–112.

Young, T. 1805 An essay on the cohesion of fluids. *Philosophical Transactions of the Royal Society of London* **95**, 65–87.